On Dynamic Modeling of PCM-Controlled Converters – Buck Converter as an Example

Teuvo Suntio, *Senior Member, IEEE*

***Abstract*— Peak-current-mode (PCM) control was published first time in open literature in 1976. The observed peculiar behavior caused by the application of PCM-control in a power electronic converter have fascinated the researchers to attempting to capture the dynamics associated to it. It is commonly assumed that the peculiar phenomena originate from the sampling process in the PCM control. A resistor is usually connected as a load, when modeling the converter dynamics and during the frequency-response measurements. The load resistor will actually dominate the frequency responses and hide the real dynamics associated to PCM control. Other measurement problems will arise from the non-modeled circuit elements dominating, especially, the high-frequency dynamic behavior of the converters. Because of these problems, the PCM models are not usually properly validated. The investigations, in this paper, show that: i) the PCM models have to be accurate also at the low frequencies for ensuring, for example, stable design of output-current-feedback-controlled converters, ii) the high low-frequency accuracy can be obtained only by means of duty-ratio gain becoming infinite at the mode limit, iii) the high-frequency accuracy of the PCM models can be obtained by means of different high-frequency extensions, iv) the key for the PCM modeling lies in the proper duty-ratio constraints, and v) the high-frequency magnitude and phase behaviors are caused by the second-harmonic-mode operation of the converter due to the frequency-response-measurement injection signal. The main objective of this paper is to show that such a modeling technique, which fully matches the above criteria, has been developed already in early 1990's and later elaborated for more general form. Validation of the dynamic models is performed by simulation, where the converter and its operational environment are perfectly known. The load-resistor effect is removed computationally for performing the complete validation. A PCM-controlled buck converter is used as an example.**

***Index Terms*—PCM control, dynamic modeling, harmonic-mode operation, duty-ratio constraints**

I. Introduction

Peak-current-mode (PCM) control of switched-mode converters was publicly introduced in 1978 [1,2], which is nowadays widely applied control method due to the beneficial features that it provides in converter dynamics and overcurrent protection as discussed in [3]. The first attempt to capture the dynamics of PCM-controlled converters was reported in 1979 [4]. The state space of the PCM-controlled converter was developed by replacing the perturbed duty ratio in the direct-duty-ratio (DDR) or voltage-mode (VM)-controlled state space by means of the duty-ratio constraints [4].

In the subsequent modeling approaches, the duty-ratio constraints are usually developed by assuming the time-averaged inductor current to be constant during the switching cycle as the consequence of sample-and-hold effect [5-17]. This assumption leads usually to the duty-ratio gain to be related to the inverse of the inductor-current up slope, which is justified by the analogy to the modulator gain under DDR control (i.e., $1/V_{\mathrm{m}}$) as in [5-10]. It is, however, clearly stated in [18,19] that the development of the duty-ratio constraints shall be performed under dynamic condition, where the derivative of the time-varying averaged inductor current is not zero. When this statement is followed strictly and properly, the obtained duty-ratio gain will become infinite at the maximum duty ratio up to which the converter can work without entering into subharmonic modes [20-26]. The infinite duty-ratio gain is also obtained in [11,12] despite the assumption of constant time-varying inductor current as a result of certain additional assumptions. As an outcome of those assumptions, the obtained duty-ratio constraints equal the constraints given in [20,21,23]. The describing function method reported in [27] leads also to the duty-ratio gain, which becomes infinite at the mode-limit duty ratio. The existence of infinite duty-ratio gain is widely disputed, because its physical existence in the power electronic converters has not been verified explicitly. There is, however, plenty of evidence, which explicitly supports its existence [20-26]. Similar infinite duty-ratio gain is observed to take place also in the PCM-controlled converters operating in discontinuous conduction mode (DCM) [28]. In DCM, the mode-limit duty ratio equals the duty ratio at which the converter enters into continuous conduction mode (CCM) [28].

The practical frequency-response measurements have indicated that the magnitude and phase behaviors of the control-related transfer functions do not match with the average-model-based predictions, but they exhibit parallel-resonant-type behavior in vicinity of half the switching frequency causing increase in the magnitude and excess phase shift. This phenomenon is assumed to be the consequence of the sample-and-hold effect caused by the sampling of the inductor current [8,9,11,12]. The associated delay function is usually computed

This paragraph of the first footnote will contain the date on which you submitted your paper for review. It will also contain support information, including sponsor and financial support acknowledgment. For example, "This work was supported in part by the U.S. Department of Commerce under Grant BS123456."

T. Suntio is with the Laboratory of Electrical Energy Engineering, Tampere University of Technology, Tampere, 33720, Finland (email: teuvo.suntio@tut.fi).

based on the sampled-data modeling principles [8,12,15-17], the modulation waveforms associated to the duty-ratio process [13] or on intuition as in [29]. The delay function is usually a transfer function of infinite order in *s*, which is transformed into a finite-order mode by using different Padé approximations [10]. As an outcome of the approximation, a resonant transfer function is usually obtained, where the parameters (i.e., damping factor and undamped natural frequency) are selected for obtaining the desired high-frequency behavior of the models. As discussed in [10], the used high-frequency extension does not comply with the original delay function. The delay function is added usually in the inductor-current feedback loop [8,10]. The presented model validations, for example, in [13,14] show clearly that the resonant circuit with properly tuned parameters would yield perfect high-frequency match between the predicted and simulation-based-measured frequency responses. **C**omprehensive discussions are provided on the inductor-current loop modeling in sampled-data domain including the application of Páde approximation in Refs. [11,12]. The final outcome of those discussions is not unfortunately given in such a manner that the reader can understand explicitly, where the sampling effect has to be placed for obtaining perfect high-frequency accuracy.

As the load resistor dominates the low-frequency part of the frequency responses in most of the published papers, the overall validation of the proposed models is impossible based on the given responses. In order to predict the impedance-based interactions correctly [30] or to design a stable output-current feedback-controlled PCM-controlled converter [31], the models have to be accurate at the low frequencies as well: Fig. 1 shows the measured output-current loop gain ($L_{\mathrm{R}}(s)$, dashed line), when a PCM-controlled buck converter is loaded with a resistor. The solid line shows the corresponding measured output-current loop gain ($L_{\mathrm{B}}(s)$), when the correct load (i.e., a storage battery) is connected at the output terminal. The increase of loop crossover frequency by two decades would lead evidently to instability, because the crossover frequency of the output-current loop would be easily higher than the switching frequency, which indicates explicitly the necessity to removing the load-resistor effect from the PCM models. The detailed analysis of the load effect can be found from [31].

In this paper, we will show that the infinite-duty-ratio-gain-based models in [11,12,20-23] will produce very accurate small-signal models from DC up to 1/5$^{\mathrm{th}}$ of the switching frequency as such, which is usually considered to be the absolute-maximum crossover frequency of the feedback loop gain as well. We will also show that the models in [8,9] will produce very accurate responses from DC to half the switching frequency as has been stated also in [13,14]. The approximate transfer functions in [8] and the investigations in this paper indicate clearly that the real duty-ratio gain in [8,9] equals the infinite-gain duty-ratio gain proposed in [11,12,20-23] as well. The infinite duty-ration gain is also clearly visible in [14] (cf. Table III: R_{e}). In addition, we will show that the infinite-gain models in [20-23] can be upgraded to produce accurate high-frequency responses with a simple resonant circuit placed in the inductor-current loop. According to the thorough investigations of this paper, the high-frequency extension in [11,12] equals the extension produced by the simple method, which is applied in this paper.

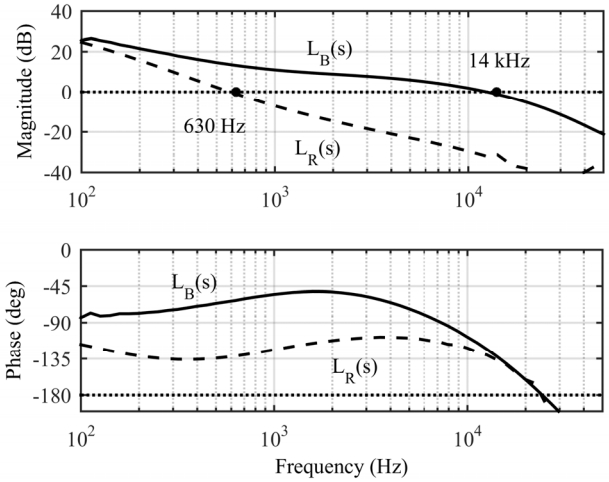

Fig. 1 Effect of resistive load on the output-current loop gain of a PCM-controlled buck converter [31].

As stated earlier, the measured small-signal behavior of the magnitude and phase of the control-related transfer functions do not correspond to the average-model-based predicted frequency responses. The investigations, in this paper, show that the mismatches are caused by the converter operation in second-harmonic mode due to the frequency-response-measurement injection signal. This operation starts gradually affecting the converter operation from 1/5$^{\mathrm{th}}$ of the switching frequency, and the duty-ratio gain F_{m} will become infinite at half the switching frequency. The measured frequency responses in vicinity of half the switching frequency are dependent on the used injection signal amplitude as well. The infinite duty-ration gain at half the switching frequency explains also why the ideal series-resonant circuit placed in the inductor-current loop improves the accuracy of the predictions as well.

The development of the small-signal models in [8,9,13-16] is rather difficult, and therefore, their application to more complicated higher-order converters would be difficult as well. The modeling methods presented in [20,23] are obtained by applying transparent modeling methodology, which produces explicit definition for the key factors in the PCM modeling i.e., the unified averaged comparator equation from which the duty-ratio constraints can be easily developed also for more complicated converters [24,25] as well as for current-fed converters [26], etc.

The main contributions of this paper are as follows: i) Confirming the real effects of PCM control on the overall dynamics of a switched-mode converter, ii) confirming the validity of the proper PCM averaged models, iii) emphasizing and verifying the necessity to removing the resistive-load effect from the analytic and measured transfer functions, iv) verifying the inductor-current loop behavior in buck converter, v) verifying the high accuracy of the models in [8,9] and the models presented in [11,12,20,21,23], and v) observing that the high-frequency magnitude and phase behaviors are caused by

the second-harmonic-mode operation of the converter due to the frequency-response-measurement injection signal. The main objective of the paper is to emphasize that the problems in PCM modeling has been successfully solved already in early 1990's in [11,20], and the modeling method is later only elaborated for more convenient and wider usage in [23]. A buck converter is used as an example for validating the accuracy of the models.

The rest of the paper is organized as follows. Section II briefly presents the PCM modeling method developed in [8,9] and [23]. Section III presents the frequency responses measured from the Matlab™ Simulink-based switching model by using pseudorandom-binary-sequence-based frequency-response measurement technique introduced in [32,33]. Experimental validation of the proposed techniques is presented in Section IV. Discussions are provided in Section V, and the conclusions are finally drawn in Section VI.

II. PCM-Control Modeling

The modeling method of the direct-duty-ratio (DDR) or voltage-mode (VM) controlled converters, which is known as state space averaging (SSA) [34,35], is known to produce accurate small-signal models up to half the switching frequency without any high-frequency modulation effects [36]. Fig. 2 shows the control-to-output-voltage frequency responses of a DDR-controlled buck converter, which are extracted from the corresponding switching model, and predicted by means of the SSA-based small-signal models (cf. e.g. [37]). The used Simulink (Matlab™) based switching models are given explicitly in [38]. Fig. 2 confirms the accuracy (i.e., perfect match) of SSA-based model as well as the absence of modulation effects. The accuracy of the DDR models is important, because the PCM models are based on them as implicitly stated in [4], whether they are developed based on the DDR state space or on the corresponding equivalent circuits [39,40] as in [8,13,14]. The high distribution of the phase-response data points in vicinity of half the switching frequency is the consequence of the used pseudorandom binary-sequence-based frequency-response measurement technique as discussed in [32,33].

The main difference between the DDR and PCM-controlled converters is that the duty ratio is generated in DRR-controlled converter by means of a fixed PWM-ramp signal and in PCM-controlled converter by means of the up slope of the instantaneous inductor current. Therefore, the small-signal models representing the dynamics of PCM-controlled converter can be established by developing the proper duty-ratio constraints of the form [4,24]

$$\hat{d} = F_{\mathrm{m}}(\hat{x}_{\mathrm{c}} - \sum_{i=1}^{n} q_{\mathrm{i}}\hat{x}_i) \tag{1}$$

where F_{m} denotes the duty-ratio gain, x_{c} the control variable, and q_i the feedback or feedforward gain related to variable x_i (i.e., state and input variables) [23,24]. The modeling is simply finalized by replacing the perturbed duty ratio ($\hat{d}$) in the small-signal state space of the corresponding DDR-controlled converter by means of (1) [37].

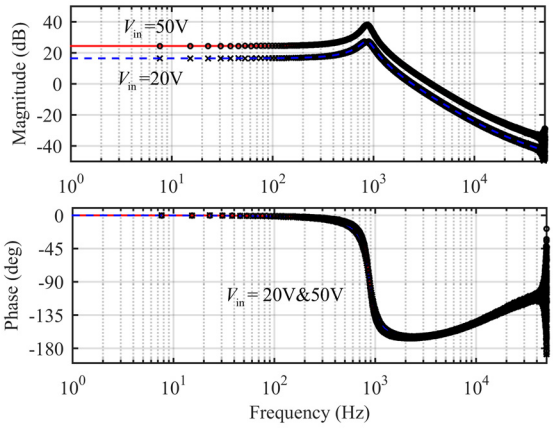

Fig. 2 Frequency responses of control-to-output-voltage of a DDR-controlled buck converter with 100-kHz switching frequency at two different input voltages: The dashed blue lines and the x-marks denote the analytically predicted and switching-model-based measurements at 20 V, and the solid red lines and the circle-marks denote the same predictions and measurements at 50 V, respectively.

A. Duty-Ratio Constraints

Fig. 3 shows the inductor-current waveforms, the control current (i_{co}), and the inductor-current compensating ramp (m_{c}) during one arbitrary cycle in CCM under dynamic conditions. As discussed in [35], the real state variables producing the dynamic behavior up to half the switching frequency are the time-averaged values of the instantaneous variables within one cycle. Fig. 3 shows clearly that at the time instant (i.e., at $t = (k+d)T_{\mathrm{s}}$), when the duty ratio is established, the variables in Fig. 3 can be linked together by

$$i_{\mathrm{co}} - m_{\mathrm{c}} dT_s = \sum_{i=1}^{n} \langle i_{\mathrm{Li}} \rangle + \Delta i_{\mathrm{L}} \tag{2}$$

which is actually known as the *comparator equation* due to what physically takes place in the PWM modulator of the converter.

The only unknown variable in (2) is Δi_{L} (cf. Fig. 3), which can be solved e.g. by the geometrical studies of the inductor-current waveforms [20], by theoretical averaging techniques as in [21] or by considering the situation in Fig. 3 to be a transient state and applying the derivative of the time-varying averaged inductor current properly as in [23] (i.e., $\Delta i_{\mathrm{L}} = \frac{1}{2} m_1 dT_{\mathrm{s}} - \frac{1}{2} dT_s \frac{d\langle i_{\mathrm{L}} \rangle}{dt}$, where $\frac{d\langle i_{\mathrm{L}} \rangle}{dt} = dm_1 - d'm_2$ (cf. [35])). As an outcome of the named techniques, Δi_{L} can be given in general [23] by

$$\Delta i_{\mathrm{L}} = \frac{dd'T_{\mathrm{s}}}{2} \left(\sum_{i=1}^{n} (m_{1i} + m_{2i}) \right) \tag{3}$$

where m_{1i} and m_{2i} denote the absolute values of the up and down slopes of the associated inductor currents as denoted in Fig. 3.

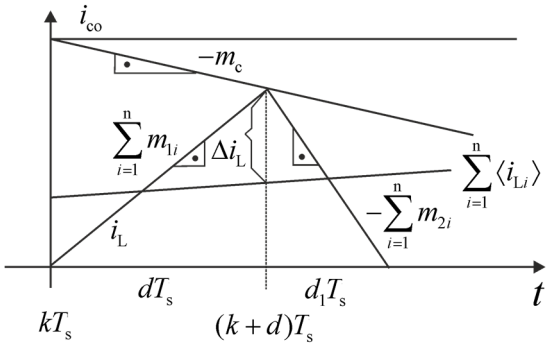

Fig. 3 Inductor-current waveforms in CCM including the control current and compensation ramp.

The different gains in the small-signal duty ratio constraints in (1) can be found by replacing the up and down slope with their topology-based values in (3) as well as linearizing the corresponding averaged comparator equation in (2) at a certain operating point. The duty-ratio gain (F_m) can be given in a generalized form by

$$F_m = \frac{1}{T_s\left(M_c + (D'-D)\dfrac{\sum_{i+1}^{n}(M_{1i}+M_{2i})}{2} \right)} \tag{4}$$

which indicates that it becomes infinite, when the duty ratio (D_{ML}) equals

$$D_{ML} = \frac{1}{2} + \frac{M_c}{\sum_{i=1}^{n}(M_{1i}+M_{2i})} \tag{5}$$

and defines the mode limit (ML) for the operation of the converter at the switching frequency. If requiring harmonic-mode-free operation of the converter in all conditions (i.e., steady state and transients) within the specified input-voltage range (i.e., up to $D_{ML}=1$) then the compensation should be designed as

$$M_c \geq \frac{\sum_{i=1}^{n}(M_{1i}+M_{2i})}{2} \tag{6}$$

The compensation value in (6) does not comply with the optimal compensation value of the buck converter, which would nullify the audiosusceptibility (i.e., $G_{io\text{-}o}=0$ in (23)). Such a compensation value can be given for the buck-type converters in general [24] by

$$M_{c\text{-}opt} = \frac{\sum_{i=1}^{n} M_{2i}}{2} \tag{7}$$

Fig. 4 shows the measured instantaneous inductor current, when the converter operates in second-harmonic mode. Fig. 4 shows clearly that the up and down slopes as absolute values are equal, when the inductor-current loop is not compensated (i.e., $M_c=0$).

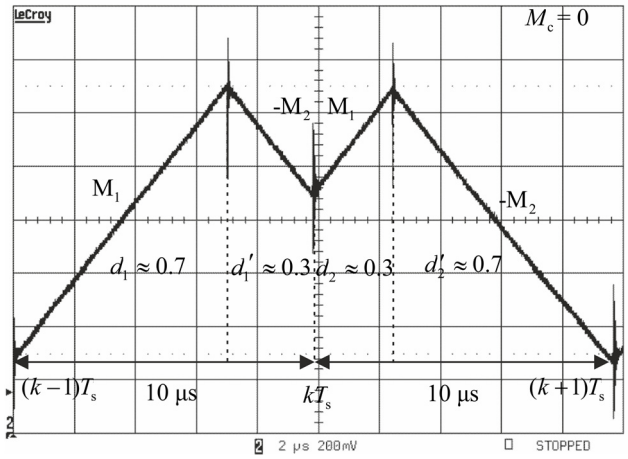

Fig. 4 The measured inductor-current waveforms in the second-harmonic-mode of operation.

The peculiar behavior of the inductor current in Fig. 4 can be explained by means of the infinite duty-ratio gain as follows: The inductor-current feedback loop and the control current form a similar constellation as the well-known voltage-follower-operational-amplifier circuit, which can be expressed as

$$\begin{aligned} \hat{i}_L &= F_m(\hat{i}_{co} - \hat{i}_L) \\ \hat{i}_L &= \frac{F_m}{1+F_m}\hat{i}_{co} \end{aligned} \tag{8}$$

According to (8), $\hat{i}_L = \hat{i}_{co}$ when $F_m = \infty$, which means that $\hat{i}_L = 0$ when $i_{co} = I_{co}$ as it is in open loop. In practice, this means that the inductor-current derivative will be zero. According to [35], the inductor-current derivative can be given in CCM by

$$\frac{d\langle i_L \rangle}{dt} = dm_1 - d'm_2 \tag{9}$$

When equating the derivative in (9) to zero and replacing the duty ratio by the mode-limit duty ratio in (5), we get the relation between the inductor-current slopes and the compensation ramp as

$$m_2 = m_1 + 2M_c \tag{10}$$

which indicate that the up and down slopes as absolute values are equal when $M_c=0$ as in Fig. 4. The existence of the even harmonic operation modes can be explained by the equality of the absolute values of the slopes, which dictates the operational frequencies to be $f_s/2^n$, where f_s denotes the switching frequency. According to the inductor-current waveforms in Fig. 4, we can compute that the corresponding averaged duty ratio can be given by

$$D_{av} = \frac{d_1+d_2}{2} = \frac{m_2}{m_1+m_2} \tag{11}$$

According to the equality in (10), we can compute the mode-limit duty ratio in (5) to be

$$D_{\mathrm{ML}} = \frac{m_2}{m_1 + m_2} \tag{12}$$

which equals the averaged duty ratio in (11). This means that the mode-limit duty ratio will govern the operation of the converter in harmonic modes [23]. More information related to the PCM control can be found from [37]. It may be obvious that the resonant-like behavior of the inductor-current loop at half the switching frequency cannot explain the harmonic behavior of the inductor current at the frequencies of $f_s / 2^n$, where n >1. Dr. Bass gave the same message already in 1990 in his PhD dissertation based on the system eigenvalues vs. the switching frequency [41].

The averaged comparator equation in (2) can be developed further in terms of duty ratio (D) in steady state for a second-order converters as follows

$$I_{\mathrm{co}} - I_{\mathrm{L}} = -\frac{(M_1 + M_2)T_{\mathrm{s}}}{2} \cdot D^2 + (M_{\mathrm{c}} + \frac{M_1 + M_2}{2})T_{\mathrm{s}} \cdot D \tag{13}$$

According to (13), we can compute that the minimum distance between the control current and average inductor current will be limited to

$$\left| I_{\mathrm{co}} - I_{\mathrm{L}} \right|_{\min} = \frac{M_{\mathrm{c}} T_{\mathrm{s}}}{2}(1 + \frac{M_{\mathrm{c}}}{M_1 + M_2}) + \frac{(M_1 + M_2)T_{\mathrm{s}}}{8} \tag{14}$$

at the duty ratio

$$D = \frac{1}{2} + \frac{M_{\mathrm{c}}}{M_1 + M_2} \tag{15}$$

which equals D_{ML} in (5) and (12). At the higher duty ratios, the comparator equation in (13) does not have any more real valued solutions. The same minimum distance is also obtained in [42] based on chaos theory. In practice, this means that the inductor-current ripple has to start increasing for continuing the operation of the converter as explicitly visible in Fig. 4. In the small-signal models, the non-existence of real valued solutions is reflected as infinite modulator gain. Thus the developed comparator equation predicts exactly the duty-ratio value, at which the converter will enter into harmonic mode of operation, when the inductor-current-loop compensation is varied.

B. Small-Signal Model of PCM-Controlled Buck Converter

The power stage of the PCM-controlled buck converter is shown in Fig. 5 with the resistive load and the values of components. According to (2) and (3) as well as the definition of the inductor-current up and down slopes (cf. [35]), the corresponding duty-ratio constraints can be given by

$$\hat{d} = F_{\mathrm{m}}(\hat{i}_{\mathrm{co}} - q_{\mathrm{L}}\hat{i}_{\mathrm{L}} - q_{\mathrm{in}}\hat{v}_{\mathrm{in}}) \tag{16}$$

where

$$\begin{aligned} F_{\mathrm{m}} &= \frac{1}{T_{\mathrm{s}}(M_{\mathrm{c}} + \frac{(D' - D)V_{\mathrm{e}}}{2L})} \\ q_{\mathrm{L}} &= 1 + \frac{DD'T_{\mathrm{s}}}{2L}(r_{\mathrm{d}} - r_{\mathrm{ds}}) \\ q_{\mathrm{in}} &= \frac{DD'T_{\mathrm{s}}}{2L} \\ V_{\mathrm{e}} &= V_{\mathrm{in}} + V_{\mathrm{D}} + (r_{\mathrm{d}} - r_{\mathrm{ds}})I_{\mathrm{o}} \end{aligned} \tag{17}$$

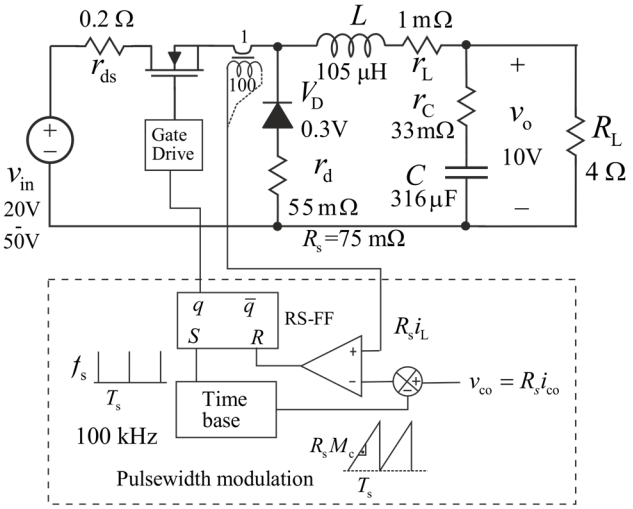

Fig. 5 The power stage of the PCM-controlled buck converter.

The set of PCM transfer functions for the basic buck, boost, and buck-boost converters can be derived in a general form from the block diagram presented in Fig. 6 based on the general duty-ratio constraints of (18). In Fig. 6, the transfer functions denoted by the superscript 'DDR' corresponds to the set of transfer functions describing the dynamic behavior of the corresponding DDR-controlled converter**.**

$$\hat{d} = F_{\mathrm{m}}(\hat{i}_{\mathrm{co}} - q_{\mathrm{L}}\hat{i}_{\mathrm{L}} - q_{\mathrm{in}}\hat{v}_{\mathrm{in}} - q_{\mathrm{o}}\hat{v}_{\mathrm{o}}) \tag{18}$$

The general set of transfer functions can be given as shown in (19) (the output dynamics) and (20) (the input dynamics), respectively.

$$\begin{aligned} G_{\text{io-o}} &= \frac{\hat{v}_{\mathrm{o}}}{\hat{v}_{\mathrm{in}}} = \frac{(1 + \frac{\mathrm{B}F_{\mathrm{m}}q_{\mathrm{L}}}{\mathrm{A}})G_{\text{io-o}}^{\mathrm{DDR}} - F_{\mathrm{m}}q_{\mathrm{in}}G_{\text{co-o}}^{\mathrm{DDR}}}{1 + L_{\mathrm{c}} + L_{\mathrm{v}}} \\ Z_{\text{o-o}} &= \frac{\hat{v}_{\mathrm{o}}}{\hat{i}_{\mathrm{o}}} = \frac{(1 + \frac{\mathrm{B}F_{\mathrm{m}}q_{\mathrm{L}}}{\mathrm{A}})Z_{\text{o-o}}^{\mathrm{DDR}} + \frac{F_{\mathrm{m}}q_{\mathrm{L}}}{\mathrm{A}}G_{\text{co-o}}^{\mathrm{DDR}}}{1 + L_{\mathrm{c}} + L_{\mathrm{v}}} \\ G_{\text{co-o}} &= \frac{\hat{v}_{\mathrm{o}}}{\hat{i}_{\mathrm{co}}} = \frac{F_{\mathrm{m}}G_{\text{co-o}}^{\mathrm{DDR}}}{1 + L_{\mathrm{c}} + L_{\mathrm{v}}} \end{aligned} \tag{19}$$

$$
\begin{aligned}
Y_{\text{in-o}} &= \frac{\hat{i}_{\text{in}}}{\hat{v}_{\text{in}}} = Y_{\text{in-o}}^{\text{DDR}} - \frac{F_{\text{m}}((q_{\text{o}} + \frac{q_{\text{L}}}{\text{A}Z_{\text{C}}})G_{\text{io-o}}^{\text{DDR}} + q_{\text{in}})G_{\text{ci-o}}^{\text{DDR}}}{1 + L_{\text{c}} + L_{\text{v}}} \\
T_{\text{oi-o}} &= \frac{\hat{i}_{\text{in}}}{\hat{i}_{\text{o}}} = T_{\text{oi-o}}^{\text{DDR}} + \frac{F_{\text{m}}((q_{\text{o}} + \frac{q_{\text{L}}}{\text{A}Z_{\text{C}}})Z_{\text{o-o}}^{\text{DDR}} - \frac{q_{\text{L}}}{\text{A}})G_{\text{ci-o}}^{\text{DDR}}}{1 + L_{\text{c}} + L_{\text{v}}} \\
G_{\text{ci-o}} &= \frac{\hat{i}_{\text{in}}}{\hat{i}_{\text{co}}} = \frac{F_{\text{m}}G_{\text{ci-o}}^{\text{DDR}}}{1 + L_{\text{c}} + L_{\text{v}}}
\end{aligned}
\tag{20}
$$

where Z_{C} denotes the impedance of the output capacitor, L_{c} and L_{v} denote the inductor-current and output-voltage loop gains as given in (21) (i.e., $G_{\text{cL-o}}^{\text{DDR}}$ and $G_{\text{co-o}}^{\text{DDR}}$ denote the control-to-inductor-current and control-to-output-voltage transfer functions of the corresponding DDR-controlled converter (cf. [37]) as well as $\text{A}=1$ and $\text{B}=0$ for a buck converter, and $\text{A}=D'$ and $\text{B}=I_{\text{L}}$ for boost and buck-boost converters, respectively.

$$
\begin{aligned}
L_{\text{c}} &= F_{\text{m}}q_{\text{L}}G_{\text{cL-o}}^{\text{DDR}} \\
L_{\text{v}} &= F_{\text{m}}q_{\text{o}}G_{\text{co-o}}^{\text{DDR}}
\end{aligned}
\tag{21}
$$

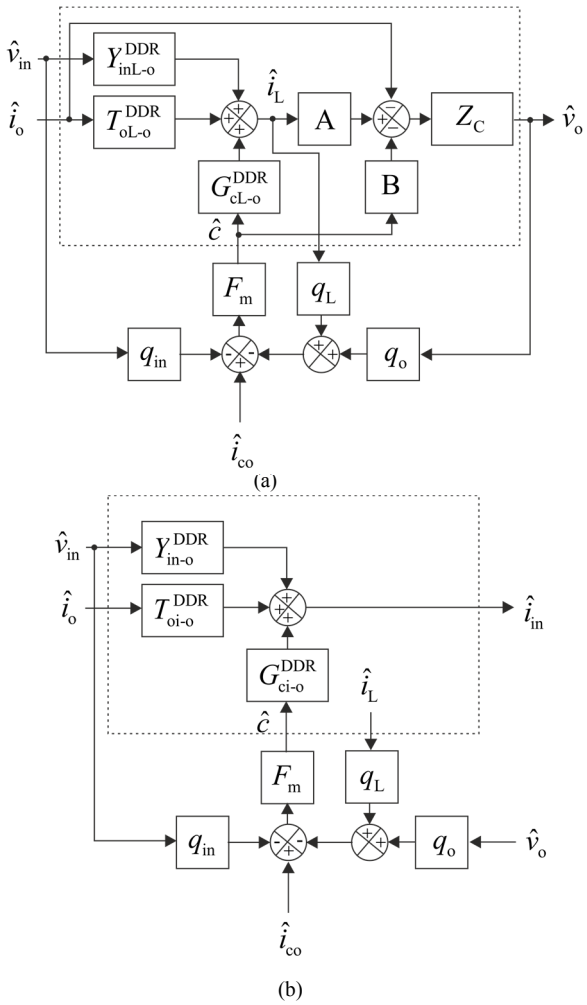

Fig. 6 The control-engineering-type block diagrams for computing the general transfer functions representing (a) the output dynamics and (b) the input dynamics of the basic second-order converters.

The explicit internal or unterminated set of transfer functions of the buck converter can be obtained by replacing $\hat{d}$ in the linearized state space of the corresponding DDR-controlled buck converter (cf. [23]) by (16). The corresponding transfer functions can be solved from the obtained linearized PCM state space (cf. [23,37]) yielding

$$
\begin{aligned}
Y_{\text{in-o}} &= \frac{\hat{i}_{\text{in}}}{\hat{v}_{\text{in}}} = \frac{(D - F_{\text{m}}V_{\text{e}}q_{\text{in}})(D - F_{\text{m}}I_{\text{o}}q_{\text{L}})s}{L\Delta} - F_{\text{m}}q_{\text{in}}I_{\text{o}} \\
T_{\text{oi-o}} &= \frac{\hat{i}_{\text{in}}}{\hat{i}_{\text{o}}} = \frac{(D - F_{\text{m}}I_{\text{o}}q_{\text{L}})(1 + sr_{\text{C}}C)}{LC\Delta} \\
G_{\text{ci-o}} &= \frac{\hat{i}_{\text{in}}}{\hat{i}_{\text{co}}} = \frac{F_{\text{m}}V_{\text{e}}(D - F_{\text{m}}I_{\text{o}}q_{\text{L}})s}{LC\Delta} + F_{\text{m}}I_{\text{o}}
\end{aligned}
\tag{22}
$$

and

$$
\begin{aligned}
Z_{\text{o-o}} &= \frac{\hat{v}_{\text{o}}}{\hat{i}_{\text{o}}} = \frac{(r_{\text{e}} - r_{\text{C}} + F_{\text{m}}V_{\text{e}}q_{\text{L}} + sL)(1 + sr_{\text{C}}C)}{LC\Delta} \\
G_{\text{io-o}} &= \frac{\hat{v}_{\text{o}}}{\hat{v}_{\text{in}}} = \frac{(D - F_{\text{m}}V_{\text{e}}q_{\text{in}})(1 + sr_{\text{C}}C)}{LC\Delta} \\
G_{\text{co-o}} &= \frac{\hat{v}_{\text{o}}}{\hat{d}} = \frac{F_{\text{m}}V_{\text{e}}(1 + sr_{\text{C}}C)}{LC\Delta}
\end{aligned}
\tag{23}
$$

where the denominator of the transfer functions is

$$
\Delta = s^2 + s\frac{r_{\text{e}} + F_{\text{m}}V_{\text{e}}q_{\text{L}}}{L} + \frac{1}{LC} \tag{24}
$$

and r_{e} and V_{e} are

$$
\begin{aligned}
r_{\text{e}} &= r_{\text{L}} + Dr_{\text{ds}} + D'r_{\text{d}} + r_{\text{C}} \\
V_{\text{e}} &= V_{\text{in}} + (r_{\text{d}} - r_{\text{ds}})I_{\text{o}}
\end{aligned}
\tag{25}
$$

For comparison, the corresponding control-to-output-voltage transfer function of the DDR-controlled buck converter can be given by

$$
G_{\text{co-o}}^{\text{DDR}} = \frac{V_{\text{e}}(1 + sr_{\text{C}}C)}{s^2LC + sr_{\text{e}}C + 1} \tag{26}
$$

for the verification of the responses shown in Fig. 2 [35,37]. The denominator in (24) indicates clearly that the PCM control will increase the damping of the system by increasing the coefficient of s by $F_{\text{m}}V_{\text{e}}q_{\text{L}}$ (cf. (24) vs. (26)), which is usually a lossless resistance of tens of ohms connected in series with the output inductor. The control-related transfer functions in (22) and (23) show that F_{m} equals also directly the modulator gain similarly as $1/V_{\text{m}}$ in the DDR-controlled converter (i.e., V_{m} equals the peak-to-peak value of the constant PWM ramp signal).

It is well known that the damping factor of the PCM-controlled converter is quite high, which means that the roots of the denominator in (24) are well separated. Therefore, they can be estimated as follows

$$
\omega_{\text{Low-freq}} \approx \frac{1}{F_{\text{m}}V_{\text{e}}q_{\text{L}}C} \quad \omega_{\text{High-freq}} \approx \frac{F_{\text{m}}V_{\text{e}}q_{\text{L}}}{L} \tag{27}
$$

which shows that the low-frequency pole moves towards the origin and the high-frequency pole moves towards infinity,

when the duty ratio approaches the value of mode limit (D_{ML}) (cf. (5)) and F_{m} approaches infinity as discussed earlier. As a consequence, the output impedance of the converter (cf. $Z_{\mathrm{o\text{-}o}}$ in (23)) at the mode limit equals the output-capacitor impedance of the converter, because the inductor will be effectively blocked by the infinite lossless series resistance (i.e., $F_{\mathrm{m}}V_{\mathrm{e}}q_{\mathrm{L}}$). Fig. 7 shows the simulation-based measured output impedances of the buck converter, when the duty ratio approaches the mode limit (i.e., $D_{22\mathrm{V}}=0.4759$ (solid red lines), $D_{21\mathrm{V}}=0.4986$ (dashed blue lines)), and passes it (V_{in} = 20.8V & 20.5V (solid and dashed black lines; 2nd harmonic modes).

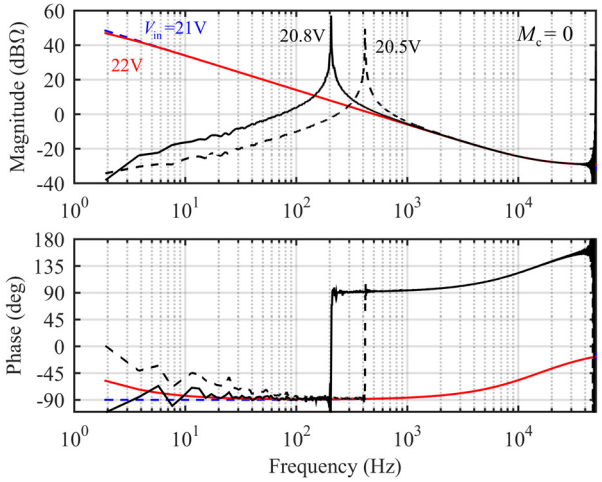

Fig. 7 Behavior of output impedance, when the duty ratio approaches the mode limit and goes beyond it.

The low-frequency phase behavior at the input voltage of 21 V (i.e., $D\approx 0.5$) shows clearly that the output impedance resembles the output-capacitor impedance at the mode limit as discussed above (i.e., the magnitude has slope of -20 dB/decade and the phase equals – 90 degrees). Fig. 7 shows that the output impedance will exhibit resonant behavior, when the converter enters into harmonic mode, where the resonant poles locate in the right half plane. The averaging-based models do not naturally explain the observed phenomenon. The internal resonance of the converter is close to 900 Hz, and therefore, the observed resonances are not related to it.

The unterminated inductor-current loop gain of the buck converter can be given by (28) (cf. (21)), because the coefficient $q_{\mathrm{o}}=0$ in case of the buck converter (cf. (17)). In case of boost and buck-boost converters, the inductor-current loop gain is affected also by the feedback from the output voltage (cf. Fig. 6a).

$$L_{\mathrm{ind\text{-}cur}}=F_{\mathrm{m}}q_{\mathrm{L}}G_{\mathrm{cL\text{-}o}}^{\mathrm{DDR}} \tag{28}$$

where the control-to-inductor-current transfer function equals

$$G_{\mathrm{cL\text{-}o}}^{\mathrm{DDR}}=\frac{V_{\mathrm{e}}sC}{s^2LC+sr_{\mathrm{e}}C+1} \tag{29}$$

When measuring the loop gain, the load impedance (Z_{L}) will affect the loop gain as

$$L_{\mathrm{ind\text{-}cur}}^{Z_{\mathrm{L}}}=F_{\mathrm{m}}q_{\mathrm{L}}\left(G_{\mathrm{cL\text{-}o}}^{\mathrm{DDR}}+\frac{T_{\mathrm{oL\text{-}o}}^{\mathrm{DDR}}}{Z_{\mathrm{L}}}\cdot\frac{G_{\mathrm{co\text{-}o}}^{DDR}}{1+\frac{Z_{\mathrm{o\text{-}o}}^{\mathrm{DDR}}}{Z_{\mathrm{L}}}}\right) \tag{30}$$

where the output-current-to-inductor-current transfer function ($T_{\mathrm{oL\text{-}o}}^{\mathrm{DDR}}$) and output impedance ($Z_{\mathrm{o\text{-}o}}^{\mathrm{DDR}}$) can be given according to [37] by

$$\begin{aligned}T_{\mathrm{oL\text{-}o}}^{\mathrm{DDR}}&=\frac{1+sr_{\mathrm{C}}C}{s^2LC+sr_{\mathrm{e}}C+1}\\ Z_{\mathrm{o\text{-}o}}^{\mathrm{DDR}}&=\frac{(r_{\mathrm{e}}-r_{\mathrm{C}}+sL)(1+sr_{\mathrm{C}}C)}{s^2LC+sr_{\mathrm{e}}C+1}\end{aligned} \tag{31}$$

Fig. 8 shows the measured and predicted frequency responses of the load-resistor-affected inductor-current loop. The measurements are performed at the input voltage of 50 V (red), 30 V (blue), and 25 V (magenta). The predicted responses are denoted by black lines (50 V: solid; 30 V: dashed, and 25 V: dash-dotted). The low-frequency part (i.e., < 100 Hz) of the responses equals $F_{\mathrm{m}}q_{\mathrm{L}}V_{\mathrm{e}}/R_{\mathrm{L}}$, which is perfectly predicted by (30). Fig. 8 shows that the magnitude and phase will start deviating from the predictions based on the average model and exhibiting series-resonant-like behavior with right-half-plane (RHP) feature. Ref. [8] shows also inductor-current-loop measurements. The author has stated that the prediction and measurement have very good match despite the small gain error (i.e., the predicted magnitude is smaller than the measured one). This actually indicate that the assumed modulator gain does not correspond to the duty-ratio gain governing the behavior of the inductor-current loop in a buck converter. The author has not recognized either that the inductor-current loop gain, in the model, will also be affected by the feedback from the output voltage (i.e., k_{r} cf. [8,9]), which would correct the prediction to match the measured response.

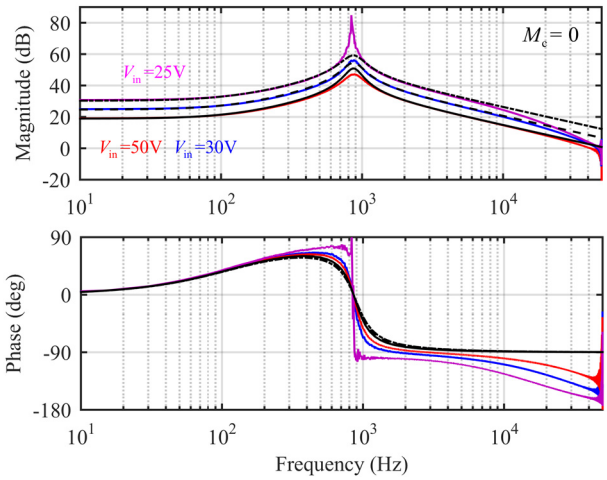

Fig. 8 The measured and predicted load-affected ($R_{\mathrm{L}}=4\Omega$) inductor-current loop gains at the input voltage of 50 V (red solid line), 30 V (blue solid line), and 25 V (magenta solid line). The predicted responses are denoted by black lines (50 V: solid line; 30 V: dashed line, and 25 V: dash-dotted line).

Fig. 9 shows the behavior of the duty-ratio gain (F_{m}) in (17), when the duty ratio approaches the mode limit value of 0.5.

According to Fig. 9, it may be obvious that the practical measurement of the infinite gain is impossible because of requiring extremely small injection signal without forcing the duty ratio to pass the mode limit. Fig. 8 shows that the passing of the mode limit has taken place already at quite low duty-ratio value at the input voltage of 25 V due to the high resonant gain of the loop. Fig. 8 proves clearly that the models referenced and presented in this paper predicts well also the behavior of the inductor-current loop gain except at the high frequencies.

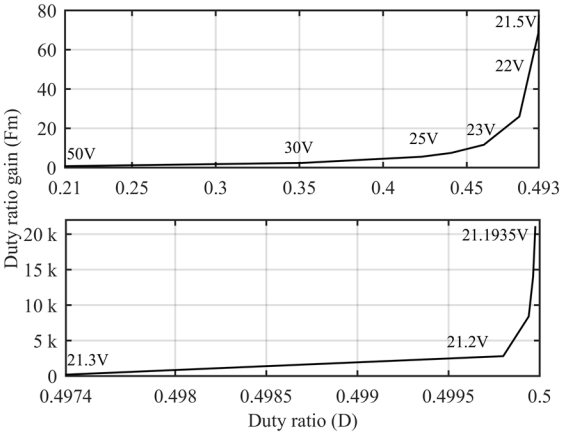

Fig. 9 The behavior of the duty-ratio gain (F_{m}), when the duty ratio approaches the mode-limit value of 0.5.

C. Buck Converter Models in Ref.[8,9]

The author of [8,9] assumes intuitively that the modulator or duty-ratio gain ($F_{\mathrm{m}}^{\mathrm{R}}$) equals $1/(m_1+M_{\mathrm{c}})/T_s$, where m_1 denotes the up slope of the inductor current and M_{c} the inductor-current-loop compensation ramp. In addition, he assumes because of the sample-and-hold effect that the time-varying average inductor current stays constant during the switching cycle. For obtaining the feedforward gain from input voltage (k_f) and the feedback gain from the output voltage (k_{r}), the author gives a comparator equation for the averaged inductor current based on geometric study of the associated waveforms as follows

$$\langle i_{\mathrm{L}}\rangle = i_{\mathrm{co}} - dT_s M_{\mathrm{c}} - \frac{d' m_2 T_{\mathrm{s}}}{2} \tag{32}$$

from which the named gains should be found by linearizing it at the operating point. Actually, the process for obtaining the gains requires additional information, which is not explicitly given in [8,9] As an outcome of the modeling process, the author gives the required gains for the buck converter as follows (Note: the load-resistor effect is removed in (33) compared to the original gains in [8,9]):

$$k_{\mathrm{f}} = -\frac{DT_{\mathrm{s}}}{L}\left(1-\frac{D}{2}\right) \quad k_{\mathrm{r}} = \frac{T_{\mathrm{s}}}{2L} \tag{33}$$

Therefore, the corresponding duty-ratio constraints for the buck converter can be given by

$$\hat{d} = F_{\mathrm{m}}^{\mathrm{R}}\left(\hat{i}_{\mathrm{co}} - (1-k_{\mathrm{r}}r_C)\hat{i}_{\mathrm{L}} + k_{\mathrm{r}}\hat{v}_{\mathrm{C}} + k_{\mathrm{f}}\hat{v}_{\mathrm{in}} - k_{\mathrm{r}}r_C\hat{i}_{\mathrm{o}}\right) \tag{34}$$

when the constraints are adapted to the state-space form (i.e., $\hat{v}_{\mathrm{o}}$ is substituted by $\hat{v}_{\mathrm{C}} + r_{\mathrm{C}}\hat{i}_{\mathrm{L}} - r_{\mathrm{C}}\hat{i}_{\mathrm{o}}$). The corresponding PCM state space can be developed similarly as in Section B by replacing the perturbed duty ratio by (34) in the DDR state space. Only the transfer functions representing the output dynamics are given here by omitting also the parasitic elements as

$$\begin{aligned} G_{\mathrm{io\text{-}o}}^{\mathrm{R}} &= \frac{D + F_{\mathrm{m}}^{\mathrm{R}} k_{\mathrm{f}} V_{\mathrm{in}}}{LC\Delta^{\mathrm{R}}} \\ Z_{\mathrm{o\text{-}o}}^{\mathrm{R}} &= \frac{sL + F_{\mathrm{m}}^{\mathrm{R}} V_{\mathrm{in}}}{LC\Delta^{\mathrm{R}}} \\ G_{\mathrm{co\text{-}o}}^{\mathrm{R}} &= \frac{F_{\mathrm{m}}^{\mathrm{R}} V_{\mathrm{in}}}{LC\Delta^{\mathrm{R}}} \\ \Delta^{\mathrm{R}} &= s^2 + s\frac{F_{\mathrm{m}}^{\mathrm{R}} V_{\mathrm{in}}}{L} + \frac{1 - F_{\mathrm{m}}^{\mathrm{R}} k_{\mathrm{r}} V_{\mathrm{in}}}{LC} \end{aligned} \tag{35}$$

Based on (35), we can compute that $G_{\mathrm{io\text{-}o}}^{\mathrm{R}} \approx 0$ when the inductor current is compensated by the optimal compensation (i.e., $M_{\mathrm{c}} = V_{\mathrm{o}}/2L$) similarly as in (23). At DC, the gain of the control-to-output-voltage transfer function ($G_{\mathrm{co\text{-}o}}^{\mathrm{R}}$) in (35) becomes

$$\frac{F_{\mathrm{m}}^{\mathrm{R}}}{1 - F_{\mathrm{m}}^{\mathrm{R}} k_{\mathrm{r}} V_{\mathrm{in}}} = \frac{1}{T_{\mathrm{s}}\left(M_{\mathrm{c}} + \frac{(D'-D)V_{\mathrm{in}}}{2L}\right)} \tag{36}$$

which equals F_{m} in (17). This means that the duty-ratio gain in the models of [8,9] becomes also infinite at the mode limit. Due to the equivalence in (36), we can expect that the models given in Subsection B and the models of [8,9] will give exactly the same frequency responses with proper high-frequency extensions.

Based on the assumption of the sample-and-hold effect to cause the observed magnitude and phase deviations in vicinity of half the switching frequency, the author of [8,9] has introduced a series-resonant circuit to be connected in the inductor-current feedback loop of the form

$$H_{\mathrm{e}}(s) = 1 + \frac{s}{Q_{\mathrm{s}}\omega_{\mathrm{s}}} + \frac{s^2}{\omega_{\mathrm{s}}^2} \tag{37}$$

where $\omega_{\mathrm{s}} = \pi/T_{\mathrm{s}}$ and $Q_{\mathrm{s}} = -2/\pi$ based on the phase behavior of the measured inductor current loop in [8,9] (cf. Fig. 8). Adding of the series-resonant element in (37) in the inductor-current loop will produce the desired effect in vicinity of half the switching frequency as will be demonstrated in Section III. If the high-frequency extension in (37) is used in the inductor-current loop given in (30) (Subsection B) then the phase shift will be much more than the measured inductor-current loops in Fig. 8 indicate.

Computing the transfer functions, where $H_{\mathrm{e}}(s)$ is included, can be most conveniently performed by means of Fig. 10 including also all the parasitic elements associated to the power stage as follows

$$Z_{\text{o-o}}^{\text{R}}=\frac{(1+\frac{\text{B}F_{\text{m}}^{\text{R}}H_{\text{e}}(s)}{\text{A}})G_{\text{io-o}}^{\text{DDR}}+\frac{F_{\text{m}}^{\text{R}}H_{\text{e}}(s)}{\text{A}}G_{\text{co-o}}^{\text{DDR}}}{1+L_{\text{c}}-L_{\text{v}}}$$

$$G_{\text{io-o}}^{\text{R}}=\frac{(1+\frac{\text{B}F_{\text{m}}^{\text{R}}H_{\text{e}}(s)}{\text{A}})G_{\text{io-o}}^{\text{DDR}}+F_{\text{m}}^{\text{R}}k_{\text{f}}G_{\text{co-o}}^{\text{DDR}}}{1+L_{\text{c}}-L_{\text{v}}} \quad (38)$$

$$G_{\text{co-o}}^{\text{R}}=\frac{F_{\text{m}}^{\text{R}}G_{\text{co-o}}^{\text{DDR}}}{1+L_{\text{c}}-L_{\text{v}}}$$

and

$$Y_{\text{in-o}}^{\text{R}}=Y_{\text{in-o}}^{\text{DDR}}-\frac{F_{\text{m}}^{\text{R}}((-k_{\text{r}}+\frac{H_{\text{e}}(s)}{\text{A}Z_{\text{C}}})G_{\text{in-o}}^{\text{DDR}}-k_{\text{f}})G_{\text{ci-o}}^{\text{DDR}}}{1+L_{\text{c}}-L_{\text{v}}}$$

$$T_{\text{oi-o}}^{\text{R}}=T_{\text{oi-o}}^{\text{DDR}}+\frac{F_{\text{m}}^{\text{R}}((-k_{\text{r}}+\frac{H_{\text{e}}(s)}{\text{A}Z_{\text{C}}})Z_{\text{o-o}}^{\text{DDR}}-\frac{H_{\text{e}}(s)}{\text{A}})G_{\text{ci-o}}^{\text{DDR}}}{1+L_{\text{c}}-L_{\text{v}}} \quad (39)$$

$$G_{\text{ci-o}}^{\text{R}}=\frac{F_{\text{m}}^{\text{R}}G_{\text{ci-o}}^{\text{DDR}}}{1+L_{\text{c}}-L_{\text{v}}}$$

where the transfer functions with the superscript 'DDR' denote the corresponding transfer functions of DDR-controlled converter, A = 1 and B = 0 for buck converter, A = D' and B = I_{L} for boost and buck-boost converters, Z_{C} denotes the impedance of the output capacitor as well as $L_{\text{c}}=F_{\text{m}}^{\text{R}}H_{\text{e}}(s)G_{\text{cL-o}}^{\text{DDR}}$ and $L_{\text{v}}=F_{\text{m}}^{\text{R}}k_{\text{r}}G_{\text{co-o}}^{\text{DDR}}$. $G_{\text{cL-o}}^{\text{DDR}}$ denotes the control-to-inductor-current transfer function of the corresponding DDR-controlled converter given in (29), and $G_{\text{co-o}}^{\text{DDR}}$ denotes the control-to-output transfer function given in (26), respectively. F_{c} equals $1/R_{\text{s}}$ (cf. Fig. 5), where R_{s} denotes the equivalent inductor-current sensing resistor, which is not included in (38) and (39) (i.e., $F_{\text{c}}=1$) (cf. Fig. 6 for comparison).

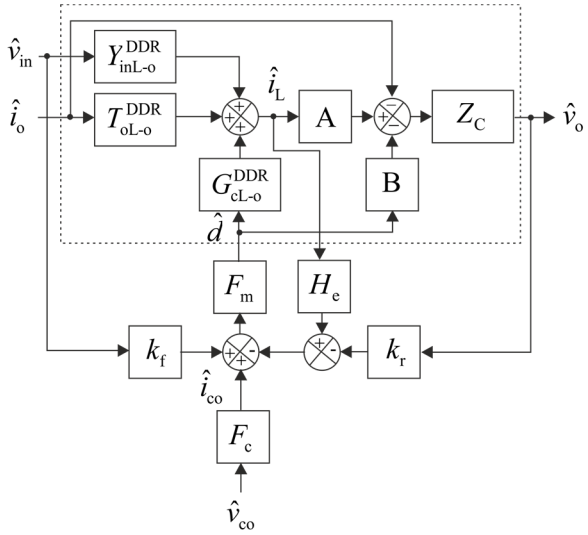

(a)

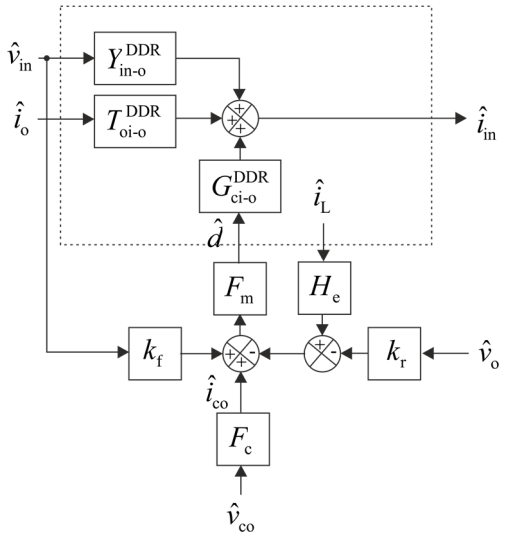

(b)

Fig. 10 Control engineering block diagrams for computing PCM transfer functions in [8,9]: (a) Output dynamics, and (b) input dynamics.

D. Load-Affected Transfer Functions

As discussed earlier, the PCM-controlled converter has to be loaded by a resistor due to its current-output nature (cf. Fig. 5), when the converter is operated in open loop [43]. Therefore, all the measured transfer functions are load resistor affected. The full set of general load-affected transfer functions of the converter can be found from [37]. We give here only the load-affected transfer functions, which we will be treat in Section III:

$$Z_{\text{o-o}}^{\text{Load}}=\frac{Z_{\text{o-o}}}{1+\frac{Z_{\text{o-o}}}{Z_{\text{L}}}} \quad G_{\text{io-o}}^{\text{Load}}=\frac{G_{\text{io-o}}}{1+\frac{Z_{\text{o-o}}}{Z_{\text{L}}}} \quad G_{\text{co-o}}^{\text{Load}}=\frac{G_{\text{co-o}}}{1+\frac{Z_{\text{o-o}}}{Z_{\text{L}}}} \quad (40)$$

The internal output impedance ($Z_{\text{o-o}}$) can be usually measured directly, but all the other transfer function will be load affected. The analytic unterminated transfer functions can be solved computationally based on the transfer functions given in (40). The process requires to using a proper software package such as Matlab™ Symbolic Toolbox. Based on (23) and (40), $G_{\text{io-o}}^{\text{Load}}$ and $G_{\text{co-o}}^{\text{Load}}$ can be given without parasitic elements by

$$G_{\text{io-o}}^{\text{Load}}=\frac{D-F_{\text{m}}V_{\text{e}}q_{\text{in}}}{LC(s^2+s(\frac{1}{R_{\text{L}}C}+\frac{F_{\text{m}}V_{\text{e}}q_{\text{L}}}{L})+\frac{1}{LC}(1+\frac{F_{\text{m}}V_{\text{e}}q_{\text{L}}}{R_{\text{L}}})}$$

$$G_{\text{co-o}}^{\text{Load}}=\frac{F_{\text{m}}V_{\text{e}}}{LC(s^2+s(\frac{1}{R_{\text{L}}C}+\frac{F_{\text{m}}V_{\text{e}}q_{\text{L}}}{L})+\frac{1}{LC}(1+\frac{F_{\text{m}}V_{\text{e}}q_{\text{L}}}{R_{\text{L}}})} \quad (41)$$

If the corresponding transfer functions are measured responses, then the computation of the unterminated responses requires to changing the measured data into complex numbers before applying (40). According to (41), the load-affected poles of the system can be given similarly as in (27) by

$$\omega_{\text{Low-freq}}^{\text{Load}}\approx\frac{1}{R_{\text{L}}C} \quad \omega_{\text{High-freq}}^{\text{Load}}\approx\frac{F_{\text{m}}V_{\text{e}}q_{\text{L}}}{L} \quad (42)$$

because $F_m V_e q_L >> R_L$. The low-frequency magnitude of $G_{co\text{-}o}^{Load}$ in (41) equals approximately R_L, and the low-frequency magnitude of $G_{io\text{-}o}^{Load}$ equals $R_L(D - F_m V_e q_{in})/(R_L + F_m V_e q_L)$, where $F_m V_e q_L$ denotes the low-frequency output impedance of the converter (cf. (23)). Thus the load resistance dominates the dynamic behavior of the converter at the low frequencies. This means also that all the different modeling methods should yield easily accurate low-frequency predictions, which do not, however, validate the model overall accuracy.

The unterminated transfer functions of the current-output PCM-controlled buck converter can be measured directly, where the load is, for example, a storage battery (cf. [30,43]). The voltage-output transfer functions can be computed as instructed in [30], which yields for the control-to-output transfer function (i.e., $G_{co\text{-}o}^{VO}$ equals $G_{co\text{-}o}$ in (23)) as

$$G_{co\text{-}o}^{VO} = \frac{G_{co\text{-}o}^{CO}}{Y_{o\text{-}o}^{CO}} \tag{43}$$

where $Y_{o\text{-}o}^{CO}$ equals $1/Z_{o\text{-}o}$ in (23). Therefore, the experimental unterminated voltage-output-mode transfer functions have to be solved computationally despite the test set up by means of which they have been obtained. According to (43), the solving of the voltage-output $G_{co\text{-}o}^{VO}$ does not require complicated transformations due to its simplicity.

III. Simulink-Based Model Validation

As stated earlier, the applied Simulink models are explicitly given in [38]. The principles of the frequency-response-analysis method is described in [32,33] and implemented as a Simulink m-file for extracting the frequency responses from the Simulink-based switching models. The pseudorandom binary-sequence technique [32,33], which is applied in extracting the frequency responses, produces rather high distribution in the data points, when the injection frequency approaches half the switching frequency as an inherent feature. The frequency response lies in the middle of the deviation band (cf. [32,33]) as it is clearly visible also in Fig. 2. The PCM models, which are introduced in Section II (i.e., (23)), are validated in Subsection A, and the models in [8,9] are validated in Subsection B, respectively.

A. Validation of PCM Models in [20,21,23]

Fig. 11 shows the set of control-to-output-voltage transfer functions, where the measured transfer functions are denoted by crosses (20V) and circles (50V). The predicted transfer functions are denoted by dashed blue lines (20V) and solid red lines (50V) (cf. (23)), respectively. The set of load-resistor-affected transfer functions ($G_{co\text{-}o}^{R_L}$) are encircled in the figure. The inductor-current loop is compensated by the optimal compensation value i.e., $M_c = V_o/2L$. The transfer functions in Fig. 11 include also the effect of the inductor-current equivalent sensing resistor (i.e., $1/R_s$).

As the figure shows, the change in the input voltage does not affect the low-frequency part (i.e., up to 5 kHz) of the load-affected transfer functions, because the load resistor dominates totally the response (cf. (41) and (42)). When the load effect is removed (cf. red and blue responses) then the real nature of the transfer functions is revealed. The model accuracy is clearly perfect at the low frequencies. It should be also observed that the magnitude of the control-to-output transfer in the frequency range from 50 Hz to 20 kHz will be stay quite constant despite the changes in the input voltage. This phenomenon is caused by the fact that the product of the low-frequency pole ($\approx 1/F_m V_{in} C$) (27) and the DC gain of the transfer function ($\approx F_m V_{in}$) will stay approximately constant ($\approx 1/C$) despite the changes in the input voltage. The same phenomenon applies also for the load-resistor-affected transfer function (i.e., $\omega_{p\text{-}LF} = 1/R_L C$ and $G_{co\text{-}o}(DC) \approx R_L$) as Fig. 11 explicitly shows. This means that the crossover frequency of the output-voltage feedback loop will stay constant despite the changes in the input voltage as well.

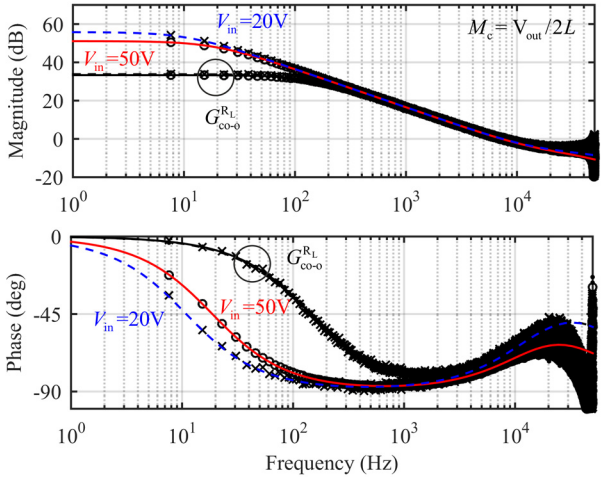

Fig. 11 The set of control-to-output-voltage transfer functions at the input voltage of 20 V (dashed blue lines, crosses) and 50 V (solid read lines, circles), where the cross and circle-marked lines denote the measured responses. The load-resistor-affected responses ($G_{co\text{-}o}^{R_L}$) are denoted by black color.

Fig. 12 shows the high-frequency part of the transfer functions in Fig. 11, which clearly indicates that the developed modeling produces very accurate responses up to 1/10th of the switching frequency without any high-frequency extension. Even at 1/5th of the switching frequency, the deviation from the real responses is very small. The modulation process starts affecting the responses significantly only after 1/5th of the switching frequency. The practical feedback-loop crossover frequency will be usually placed at the frequencies lower than 1/5th of the switching frequency, which is well covered by the developed models. The behavior of the high-frequency pole will explain part of the high-frequency phase behavior very well as discussed in Section II (i.e., the high-frequency pole will move towards infinity, when the input voltage decreases (cf. (27)).

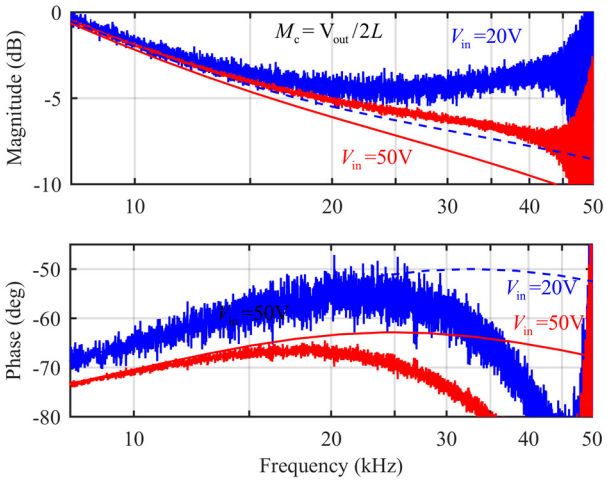

Fig. 12 The high-frequency part (i.e., from 8 kHz to 50 kHz) of the transfer functions in Fig. 11 (The red color denotes responses at 50 V, and the blue color denotes the responses at 20 V).

Figure 13 shows the set of unterminated open-loop output impedances, where the denotations are the same as in Fig. 11. As discussed earlier, the internal output impedances can be measured directly, and therefore, only the unterminated output impedances are given explicitly. The low-frequency behavior of the load-resistor-affected output impedance equals the behavior of the load-resistor-affected control-to-output-voltage transfer functions in Fig. 11. The high-frequency behavior equals the behavior of the unterminated responses in Fig. 13 (cf. Fig. 11). Fig. 13 indicates that the developed model predicts exactly the behavior of the output impedance from the low to high frequencies. In the buck converter, there are no modulation effects visible, when approaching half the switching frequency.

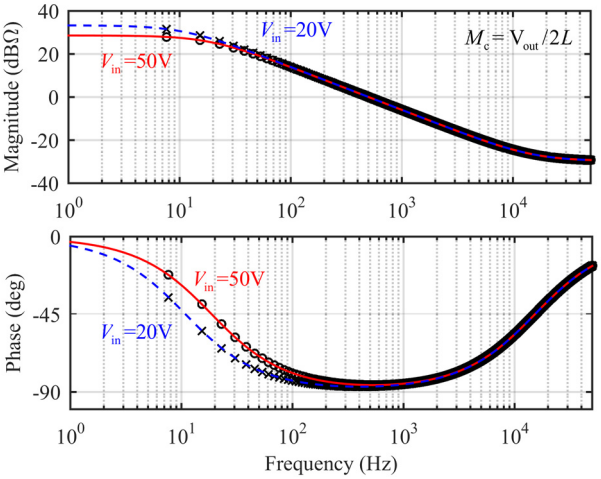

Fig. 13 The set of unterminated open-loop output impedances at the input voltage of 20 V (dashed blue lines, crosses) and 50 V (solid red line, circles), where the cross and circle-marked lines denote the measured responses.

Fig. 14 shows the set of input-voltage-to-output-voltage transfer functions ($G_{\text{io-o}}$) (i.e., audio susceptibility), where the denotations are the same as in Fig. 11. The inductor-current-loop compensation is set to zero (i.e., $M_c = 0$), because with the optimal compensation the high-frequency attenuation is so high that even Matlab™-based frequency-response analyzer cannot exactly measure the high-frequency phase behavior. The minimum input voltage is also chosen to be 22 V, because the duty ratio is higher than 0.5 at the input voltage of 20 V. The named problem is visible clearly in Fig. 14, where the phase deviation between the predicted and measured frequency responses is higher than expected and starting already close to 1 kHz. We can, however, expect that the model prediction would be accurate up to 1/10th of the switching frequency as in the case of $G_{\text{co-o}}$ in Fig. 11. The additional attenuation effect of the resistive load is also clearly visible in Fig. 14 as discussed in Section II (cf. The responses denoted by $G_{\text{io-o}}^{\text{R}_\text{L}}$).

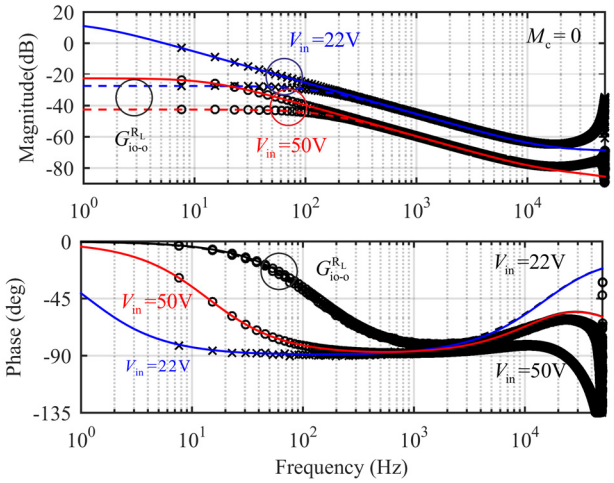

Fig.14 The set of open-loop input-to-output transfer functions at the input voltage of 20 V (blue lines, crosses) and 50 V (red lines, circles), where the cross and circle-marked lines denote the measured responses. The load-resistor-affected responses are denoted by $G_{\text{io-o}}^{\text{R}_\text{L}}$.

The high-frequency accuracy of the models in (22) and (23) can be improved by adding an ideal series- resonant circuit in the inductor-current feedback loop similarly as in the modeling method of [8,9]. The resonant circuit will be of the form

$$H_{\text{sr}}(s) = 1 + \frac{s^2}{\omega_{\text{sr}}^2} \tag{44}$$

where $\omega_{\text{sr}} = \pi / T_{\text{s}}$ (i.e., half the switching frequency). If using the similar series-resonant circuit as the author of [8,9] in (37) then the phase shift would be decreased, because the series-resonant circuit will be sitting in the denominator of the transfer functions as shown in (45) and (46) (i.e., $L_{\text{c}} = F_{\text{m}} H_{\text{sr}} q_{\text{L}} G_{\text{cL-o}}^{\text{DDR}}$). The corresponding models can be computed by replacing q_{L} with $q_{\text{L}} H_{\text{sr}}(s)$ in (19)-(21), which can be given by (cf. [37])

$$Y_{\text{in-o}} = Y_{\text{in-o}}^{\text{DDR}} - \frac{F_{\text{m}}((q_{\text{o}} + \frac{H_{\text{sr}}(s)q_{\text{L}}}{\text{A}Z_{\text{C}}})G_{\text{in-o}}^{\text{DDR}} + q_{\text{in}})G_{\text{ci-o}}^{\text{DDR}}}{1 + L_{\text{c}} + L_{\text{v}}}$$

$$T_{\text{oi-o}} = T_{\text{oi-o}}^{\text{DDR}} + \frac{F_{\text{m}}((q_{\text{o}} + \frac{H_{\text{sr}}(s)q_{\text{L}}}{\text{A}Z_{\text{C}}})Z_{\text{o-o}}^{\text{DDR}} - \frac{H_{\text{sr}}(s)q_{\text{L}}}{\text{A}})G_{\text{ci-o}}^{\text{DDR}}}{1 + L_{\text{c}} + L_{\text{v}}}$$

$$G_{\text{ci-o}} = \frac{F_{\text{m}}G_{\text{ci-o}}^{\text{DDR}}}{1 + L_{\text{c}} + L_{\text{v}}} \tag{45}$$

and

$$Z_{\text{o-o}} = \frac{(1 + \frac{\text{B}F_{\text{m}}H_{\text{sr}}(s)q_{\text{L}}}{\text{A}})G_{\text{io-o}}^{\text{DDR}} + \frac{F_{\text{m}}H_{\text{sr}}(s)q_{\text{L}}}{\text{A}}G_{\text{co-o}}^{\text{DDR}}}{1 + L_{\text{c}} + L_{\text{v}}}$$

$$G_{\text{io-o}} = \frac{(1 + \frac{\text{B}F_{\text{m}}H_{\text{sr}}(s)q_{\text{L}}}{\text{A}})G_{\text{io-o}}^{\text{DDR}} - F_{\text{m}}q_{\text{in}}G_{\text{co-o}}^{\text{DDR}}}{1 + L_{\text{c}} + L_{\text{v}}} \tag{46}$$

$$G_{\text{co-o}} = \frac{F_{\text{m}}G_{\text{co-o}}^{\text{DDR}}}{1 + L_{\text{c}} + L_{\text{v}}}$$

The application of $H_{\text{sr}}(s)$ in case of buck converter (i.e., $G_{\text{co-o}}$ in (46)) will produce a second-order resonant circuit shown in (47), which will generate the desired magnitude and phase behavior, when the operating point moves towards the mode limit by modulating the damping factor ($\zeta = \frac{\omega_{\text{rs}}L}{2F_{\text{m}}V_{\text{in}}}$) of the resonant circuit i.e., $\zeta = 0$ at the mode limit, when $F_{\text{m}} = \infty$. The accuracy of the extended models in (46) is demonstrated in Subsection B.

$$\text{G}_{\text{co-o}}^{\text{HF}} \approx \frac{r_{\text{C}}}{\frac{s^2}{\omega_{\text{sr}}^2} + s\frac{L}{F_{\text{m}}V_{\text{in}}} + 1} \tag{47}$$

A thorough study of [11,12], reveals that the high-frequency extension in (47) corresponds exactly to the high-frequency extension given in [11,12] (i.e., Eq. (22)). Therefore, the validation of the models presented in this subsection and Subsection B will be valid also for the models given in [11,12]. It is later shown in Section V that F_{m} will approach infinity when the injection frequency of the frequency-response-measurement process approaches half the switching frequency due to the second-harmonic mode operation of the converter.

B. Validation of PCM Models in [8,9]

The output impedance predicted by the model in (39) will give exactly the same responses as given in Fig. 13. It is sometimes complained that the author has removed the high-frequency extension from his approximate model in [8,9], when noticing that the modulation effect does not appear in the measurement. The full-scale model, however, indicate that the high-frequency extension does not have effect on the output impedance.

Fig. 15a shows the control-to-output-voltage responses at the input voltage of 20 V (blue) and 50 V (red). The predicted responses are denoted by solid blue and red lines and the measured responses are denoted by black crosses and circles, respectively. Fig. 15b shows the high-frequency part (i.e., from 8 kHz to 50 kHz) of the responses, where the measured responses are denoted by black lines. Fig. 15 clearly indicates that the model in [8,9] exactly captures both the low and high-frequency behavior of the transfer functions. Fig. 16 shows the comparison of [8,9] model (solid blue and red lines) and the improved model (dashed black lines) of this paper in the same conditions as in Fig. 15. Fig. 16 indicates that the responses coincide perfectly. It validates also the feasibility of the high-frequency series-resonant circuit in (44). As stated in Subsection A, the models given in [11,12] will yield the same responses as the improved models of this paper.

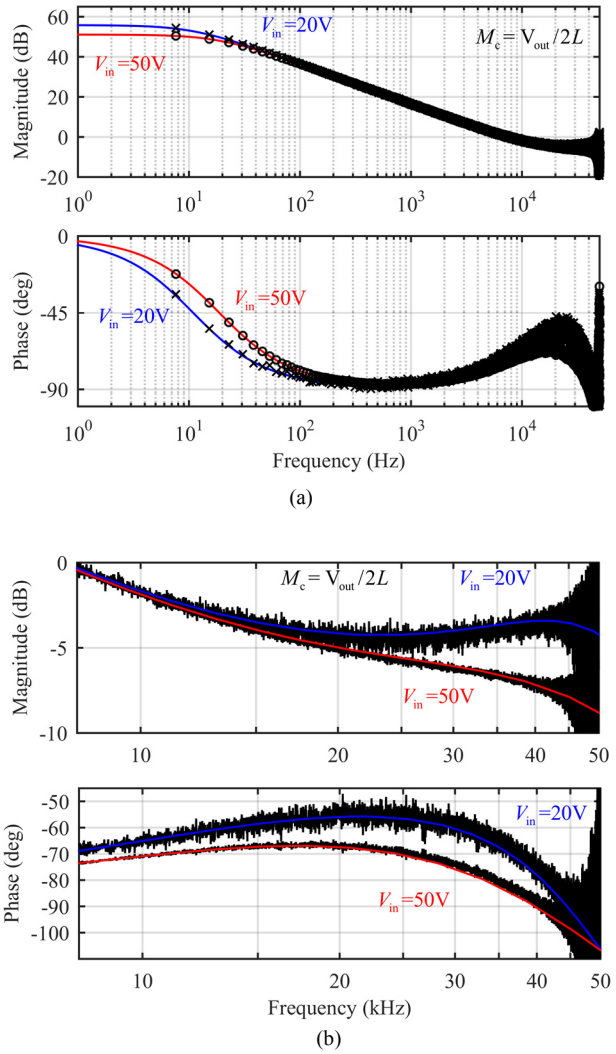

Fig. 15 [8,9]-model-based predicted (solid red and blue lines) and simulation-based measured (black lines) control-to-output-voltage responses at the input voltage of 20 V (blue) and 50 V (red): (a) the frequencies from 1 Hz to 50 kHz, and (b) the frequencies from 8 kHz to 50 kHz.

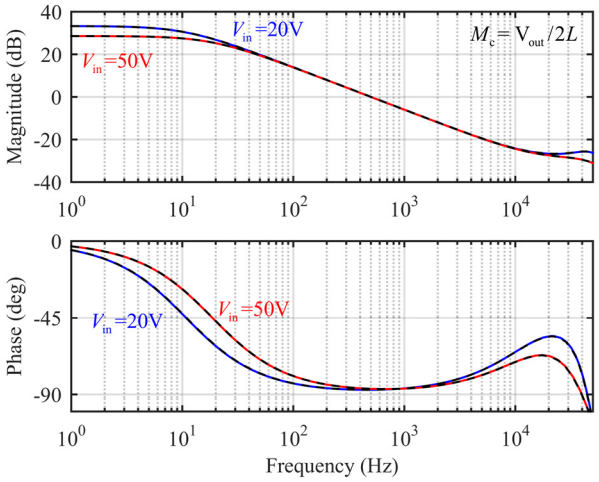

Fig. 16 The comparison of control-to-output-voltage responses predicted by [8,9]-model (blue and read solid lines) and the model of this paper with the high-frequency extension (black dashed lines).

IV. Experimental Validation

Fig. 17 shows the experimentally measured (solid lines) and predicted (dashed lines) control-to-output-voltage transfer function of the buck converter in Fig. 5. The original measurements include naturally the effect of the load resistor, which is removed computationally. Fig. 17 shows clearly that the measurement setup contains either at input or output-terminal side un-modeled circuit elements, which makes the model validation very difficult as discussed earlier. Similar high-frequency behavior is visible also in [15]. The predictions do not contain the high-frequency extension ($H_{sr}(s)$) in (47).

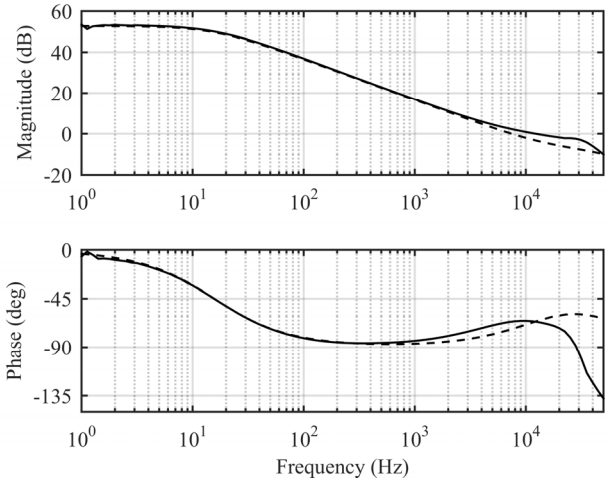

Fig. 17 The experimentally measured (solid lines) and predicted (dashed lines) control-to-output-voltage transfer functions of the buck converter in Fig. 5 at the input voltage of 20 V.

Fig. 18 shows the experimentally measured (solid lines) and predicted (dashed lines) output impedance of the buck converter. It was earlier demonstrated that the averaging-based small-signal model will predict exactly the output impedance, but that is not evident based on the given responses in Fig. 18 due to the extra circuit elements either at output or input-terminal side.

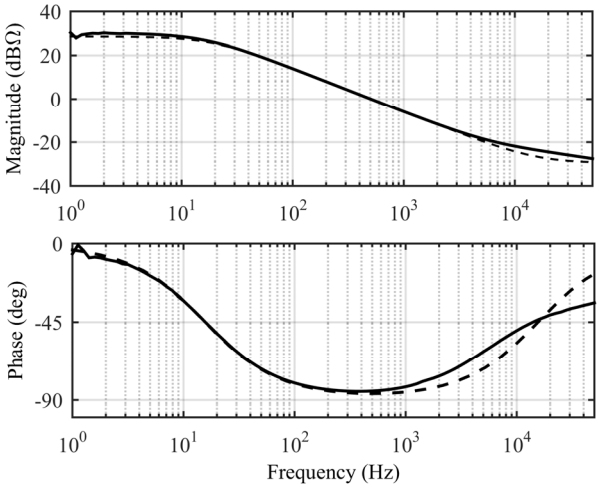

Fig. 18 The experimentally measured (solid lines) and predicted (dashed lines) output impedance of the buck converter in Fig. 5 at the input voltage of 20 V.

Fig. 19 shows the measured unterminated output-voltage feedback loops of the DDR and PCM-controlled buck converters (cf. Fig. 5) at the input voltages of 20 V (blue) and 50 V (red). The loop crossover frequencies have been designed to be equal at the input voltage of 50 V (i.e., 11 kHz) as shown in Fig. 19 (cf. the read curves). The lowering of the input voltage to 20 V reduces the crossover frequency of the DDR-controlled converter to 5.5 kHz due to the reduction of the loop magnitude by 8 dB. The crossover frequency of the PCM-controlled converter stays at 11 kHz and the loop behavior does not change at the frequencies higher than100 Hz as shown in Fig. 19 (i.e., the blue and red solid-line responses coincide). The feedback-loop gain behavior of the PCM-controlled buck converter, in Fig. 19, validates explicitly the discussions in Subsection A. This phenomenon is one of the beneficial features the PCM control will provide as well.

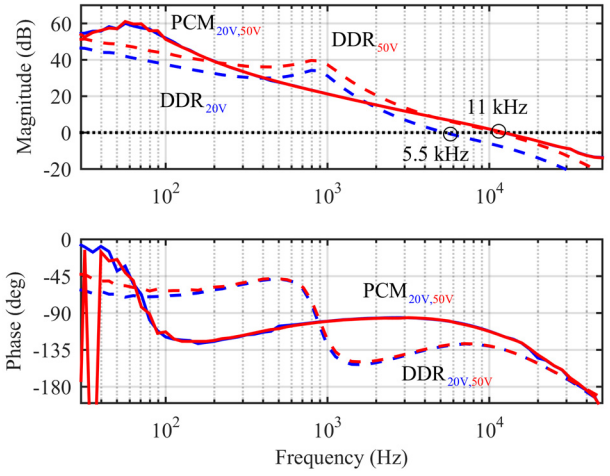

Fig. 19 The measured output-voltage feedback loops of DDR (dashed lines: 50V (red), and 20V (blue)) and PCM (solid lines: 50V (red), and 20V (blue)) PCM-controlled buck converters at the input voltage of 50 V and 20 V.

V. DISCUSSIONS

A. Sensitivity to High-Frequency Noise

The sensitivity to subharmonic oscillation and instability of the PCM-controlled converter is extensively treated recently in the open literature [44-46]. The same phenomenon is observed to take place in the DDR-controlled converters as well [47]. It is also known that the controller of the PCM-controlled converter can be based on proportional-integral-type (PI) controller because of the first-order-like system behavior (cf. Fig. 17). In power electronics, the used PI controller (i.e., Type 2) includes an extra high-frequency pole to remove the effect of switching-frequency noise as shown in [27]. The high-frequency pole has also other duties such as providing sufficient high-frequency gain margin as well as tuning the phase margin to be proper. The sensitivity studies e.g. in [44] have been performed by using the control-engineering-like PI controller, where the high-frequency pole is omitted.

Fig. 20 shows the behavior of the output-voltage feedback loop of a PCM-controlled buck converter, when the control system is based on Type 2 controller (solid line) and on control-engineering-like PI controller (dashed line). A typical feature of the PCM-controlled loop gain is the increasing of the high-frequency magnitude due to the moving of the high-frequency pole into infinity, when the operating point approaches the mode limit. To avoid the problems, the high-frequency pole has to be placed in such a manner that sufficient gain margin exists. Another role of the high-frequency pole is in adjusting the phase margin for obtaining feasible transient behavior.

The dashed line, in Fig. 20, shows that the converter will be prone to high-frequency noise effects due to the lack of sufficient gain margin. In addition, the phase margin is rather high, which would make the transient response to be very slow as well. In practice, it may be obvious that the crossover frequency has to be much lower in case of control-engineering-like PI controller than in case of Type-2 controller for obtaining robust stability (i.e., sufficient gain margin). The necessity to use the high-frequency pole will actually remove the problems associated to the switching-frequency noise.

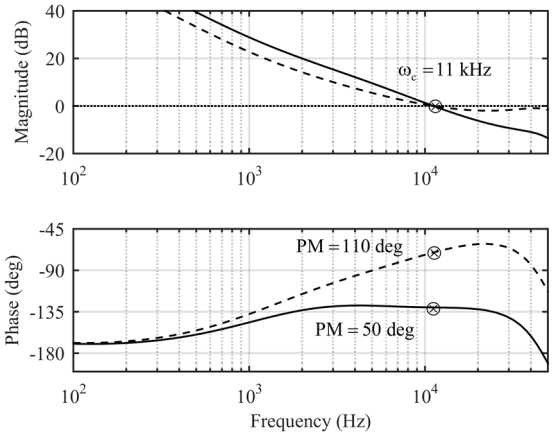

Fig. 20 The output-voltage loop gains of PCM-controlled buck converter with the use of Type-2 controller (solid lines) and control-engineering-like PI controller (dashed line).

B. Summary of Model Differences and Similarities

The existence of the infinite duty-ratio gain in the models of [8,9] and this paper including also [12,20,21] is confirmed explicitly. The author of [8,9] does not agree this fact. The models for the basic buck, boost, and buck-boost converters in [8,9] require the use a feedforward gain from the input voltage (k_f) and a feedback gain from the output voltage (k_r) for all the converters (cf. Fig. 10 and Table I). The models of this paper requires the use of only one feedforward gain (q_{in}) from the input voltage in case of the buck converter (cf. Fig. 6 and Table II). The feedback and feedforward gains for the basic converters for the models in [8,9] are given in Table I, and for the models of this paper in Table II, respectively.

The inductor-current feedback loop was measured in case of buck converter (cf. Fig. 8). The measurement shows that the model of this paper accurately models the behavior of the loop gain up to the resonant frequency and beyond. In the measured frequency responses in [8,9], the accuracy was not good, and the reason for this is that the author had not taken into account that the contribution of the feedback from the output voltage via k_r. This actually indicates that the model of this paper shows explicitly that there is no feedback from the output voltage either, because the feedback gain (q_o) equals zero (cf. Table II). In the models of this paper, the feedforward or feedback gain appears from the terminal, where the inductor current is not continuous (cf. Table II). In case of boost and buck-boost converters, the measured inductor-current loop would contain the effect of the output-voltage feedback as well.

Table I: Feedforward and feedback gains for buck, boost, and buck-boost converters in [8,9].

	Buck	Boost	Buck-boost
k_f	$-\frac{DT_s}{L}(1-\frac{D}{2})$	$-\frac{T_s}{2L}$	$-\frac{DT_s}{L}(1-\frac{D}{2})$
k_r	$\frac{T_s}{2L}$	$\frac{D'^2T_s}{2L}$	$\frac{D'^2T_s}{2L}$

Table II: Feedforward and feedback gains for buck, boost, and buck-boost converters in [12,20,21,23].

	Buck	Boost	Buck-boost
q_{in}	$\frac{DD'T_s}{2L}$	0	$\frac{DD'T_s}{2L}$
q_o	0	$\frac{DD'T_s}{2L}$	$\frac{DD'T_s}{2L}$

The major difference between the modeling methods introduced in [8,9] and this paper is how the modeling is performed in practice. The explicit procedure to obtain the required feedforward and feedback gains are not given in general form in [8,9]. The method used in this paper is explicitly given in general form in Eqs. (1)-(3), which can be applied to an arbitrary converter with ease.

As stated explicitly earlier, the models given in [11,12] are the same as reviewed in this paper. The papers contain,

however, elements, which do not promote the wider acceptance of their outcomes. The main such elements are i) the ambiguity in developing the model (i.e., from Eq. (2) to Eq. (4)) , ii) the lack of comprehensive validation of the models, and iii) the lack of explicit information, where the sampling effect shall be placed for obtaining the models.

C. *Absence of Modulation Effect in Output Impedance*

According to [8,9] and the investigations earlier in this paper, the modulation effect is not visible in the output impedance (cf. Fig. 13). Fig. 21 shows the simulation-based measurements of the input admittance of the converter without (cf. solid lines) and with an added input capacitor of 10 μF with an ESR of 30 mΩ (cf. dashed lines). As the figure shows, the added input capacitor removes the modulation effects, which is quite obvious, when it dominates fully the high-frequency behavior of the input admittance. The same applies to the absence of the modulation effects in the output impedance. In the output-impedance models (cf. $Z_{o\text{-}o}$ in (46)), the high-frequency extension ($H_{sr}(s)$) is present both in the numerator and denominator (i.e., L_c), which cancels the modulations effect to be visible in the predicted output-impedance response. This indicates also that the modulation effect is actually not a part of F_m (cf. [12]) but a part of the inductor-current loop as in [8]. If the modulation effect would a part of F_m then the modulation effect would not be visible in the control related transfer functions (cf. (46)) similarly as in $Z_{o\text{-}o}$.

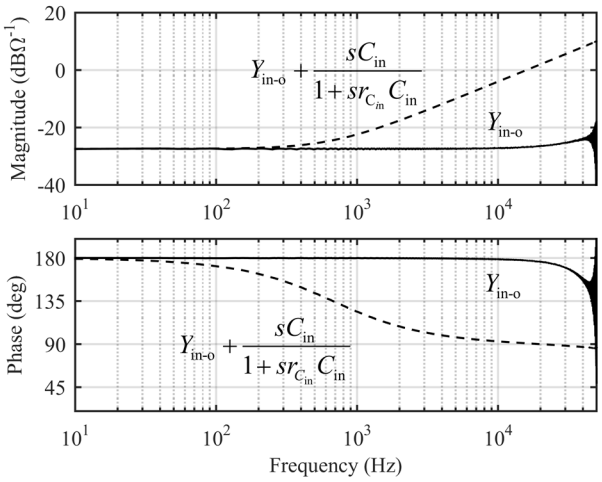

Fig. 21 The effect of input capacitor on the behavior of the input admittance.

D. *Origin of High-Frequency Behavior of Transfer Functions*

Fig. 22 shows the behavior of the output-voltage ripple, when the frequency-response injection signal is added at the control current, when measuring the frequency response of the control-to-output-voltage transfer function. Figs. 22a and 22b show that the converter operates normally (i.e., no second-harmonic operation is visible in the waveforms). Figs. 22c and 22d show that the converter enters time to time into the second harmonic mode. Fig. 22f shows that the converter operates fully in the second-harmonic operation mode, where the duty-ratio gain will be infinite. Fig. 22f shows also that the output voltage has decreased approximately by 250 mV due to the reduction in the average inductor current. Fig. 23 shows two switching cycles of the inductor current, where the modulation process is visible.

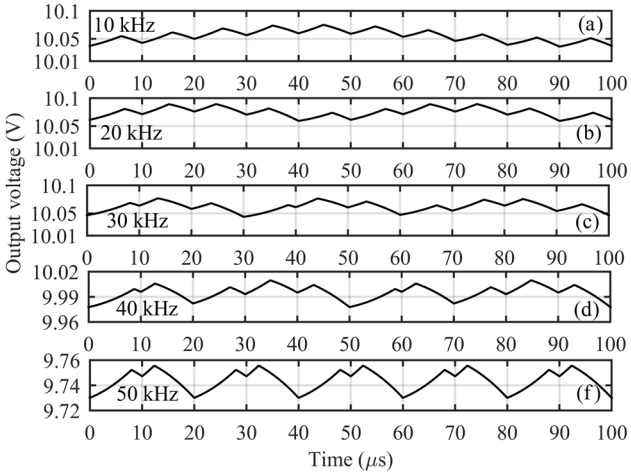

Fig. 22 Behavior of output voltage when an frequency-response injection signal is added at the control current having amplitude of 0.2 A: (a) $f_{if}=10$ kHz , (b) $f_{if}=20$ kHz , (c) $f_{if}=30$ kHz ,(d) $f_{if}=40$ kHz , and (d) $f_{if}=50$ kHz .

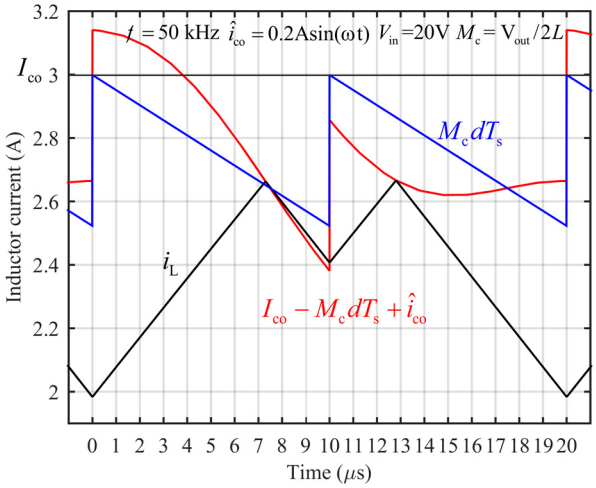

Fig. 23 Modulation process of the inductor current at half the switching frequency.

Fig. 24 shows the effect of injection-signal amplitude on the measured high-frequency part of the control-to-output-voltage transfer function, where the black solid line denotes the predicted response by using the models given in this paper, and $\hat{i}_{co}$ denotes the amplitude of the used injection signal. The figure shows that the mismatch with the prediction starts in vicinity of 1/5th of the switching frequency, which explains also why the average-model-based predictions are rather accurate up to 1/5th of switching frequency as discussed in Section III. The reason is also clearly visible in Figs. 22a and 22b.

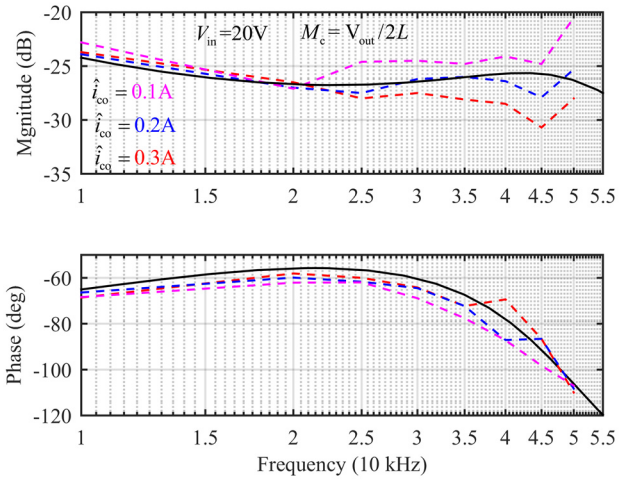

Fig. 24 Effect of the injection-signal amplitude ($\hat{i}_{co}$) on the measured high-frequency control-to-output-voltage transfer function.

VI. Conclusions

PCM control was publicly reported in the middle of 1970's and noticed to change the converter dynamic behavior profoundly compared to corresponding DDR or VM-controlled converter. The dynamic modeling to capture the dynamics related to the PCM control in CCM has fascinated the researchers for a long time. The first models, which are shown to produce highly accurate responses, are developed in late 1980's and gained high popularity later. Multitude of modeling attempts have been proposed since late 1980's, which are claimed to produce equal model accuracy or even better. Most of the presented models have been load-resistor affected, which hides, especially, the low-frequency part of the models. Therefore, the model validation has been concentrated on the frequencies close to half the switching frequency, where the unmodeled circuit elements in the test setups, the uncertainties in the component values, the state of inductor-current-feedback-loop compensation, and the effect of the frequency-response-injecting-signal level would make the validation challenging. A modeling technique, which produces such a modulator gain that becomes infinite at the mode limit, was proposed in two articles in early 1990's [11,20]. The validity of the modeling technique was categorically disputed, because the existence of the high gain was not verified in practice.

The investigations of this paper show evidently that the accurate small-signal modeling of PCM control in CCM (i.e., from DC to half the switching frequency) requires to using such duty-ratio constraints, which exhibit infinite duty-ratio gain at the mode-limit duty ratio as well as a proper high-frequency extension. It was verified that the popular models [8,9] contain also the infinite duty-ratio gain, but it is implicitly embedded in the model structures needing computational actions to revealing its existence. The infinite duty-ratio gain predicts exactly the duty ratio at which the converter enters into subharmonic mode. In addition, it can be used to predict and explain the peculiar behavior of the inductor-current up and down slopes, when the converter operates in harmonic modes. In practice, the maximum feedback-loop crossover frequency has to be placed at the frequencies less than 1/5th of the switching frequency to avoid the switching ripple to cause instability. The investigations, in this paper, show explicitly that the proper average-model-based small-signal models yield accurate predictions up to 1/5th of the switching frequency without any additional high-frequency correction.

The investigations, in this paper, shows also explicitly that the peculiar magnitude and phase behavior of the transfer functions is caused by the converter operation in harmonic mode, which is induced by the frequency-response-measurement injection signal. At half the switching frequency, the converter is permanently in second-harmonic mode, where the duty-ratio gain becomes infinite as well.

References

[1] C. W. Deisch, 'Simple switching control method changes power converter into a current source,' in *Proc. IEEE PESC*, 1978, pp. 300-306.

[2] A. Capel, G. Ferrante, D. O'Sullivan, and A. Weinberg, 'Application of injected current model for the dynamic analysis of switching regulators with the new concept of LC^3 modulator,' in *Proc. IEEE PESC*, 1978, pp. 135-147.

[3] R. Redl and N. O. Sokal, 'Current-mode control, five different types, used with the three basic classes of power converters: Small-signal ac and large-signal DC characterization, stability requirements, and implementation of practical circuits,' in *Proc. IEEE PESC*, 1985, pp. 771-785.

[4] S.-P. Hsu, A Brown, L. Rensink, and R. D. Middlebrook, 'Modeling and analysis of switching frequency of switching DC-to-DC converters in constant-frequency current programmed mode,' in *Proc. IEEE PESC*, 1979, pp. 248-301.

[5] R. D. Middlebrook, 'Modelling a current-programmed buck regulator,' in *Proc. IEEE APEC*, 1987, pp. 3-13.

[6] R. D. Middlebrook, 'Topics in multiple-loop regulators and current-mode programming,' *IEEE Trans. Power Electron.*, vol. PE-2, no. 2, pp. 109-124, Apr. 1987.

[7] R. D. Middlebrook, 'Modeling current-programmed buck and boost regulators,' *IEEE Trans. Power Electron.*, vol. 4, no. 1, pp. 36-52, Jan. 1989.

[8] R. B. Ridley, 'A new continuous-time model for current-mode control,' *IEEE Trans. Power Electron.*, vol. 6, no. 2, pp. 271-280, Apr. 1991.

[9] R. B. Ridley, *A New Small-Signal Model to Current-Mode Control,* PhD Dissertation, Virginia Polytechnic Institute and State University, 1990.

[10] R. Tymerski and D. Li, State-space models for current programmed pulsewidth-modulated converters,' *IEEE Power Electron*., vol. 8, no. 3, pp. 271-278, Jul. 1993.

[11] F. D. Tan, and R. D. Middlebrook, 'Unified modeling and measurement of current-programmed converters,' in *Proc. IEEE PESC*, 1993, pp. 380-387.

[12] F. D. Tan, and R. D. Middlebrook, 'A unified model for current-programmed converters,' *IEEE Trans. Power Electron.*, vol. 10, no. 4, pp. 397-408, Jul. 1995.

[13] J. Li and F.C. Lee, 'New modeling approach and equivalent circuit representation for current-mode control,' *IEEE Trans. Power Electron.*, vol. 25, no. 5, pp. 1218-1230, May 2012.

[14] Y. Yan, F. C. Lee, and P. Mattavelli, 'Unified three-terminal switch model for current mode controls,' *IEEE Trans. Power Electron.*, vol. 27, no. 9, pp. 4060-4070, Sep. 2012.

[15] S. C. Smithson and S. S. Williamson, 'A unified state-space model of constant-frequency current-mode-controlled power converters in continuous conduction mode,' *IEEE Trans. Ind. Electron.*, vol. 62, no. 7, pp. 4514-4524, Jul. 2015.

[16] S. Amir, R. van der Zee, and B. Nauta, 'An improved modeling and analysis technique for peak current-mode control-based boost converters,' *IEEE Trans. Power Electron.*, vol. 30, no. 9, pp. 5309-5317, Sep. 2015.

[17] N. Kondrath and M. K. Kazimierczuk, 'Control-to-output and duty-ratio-to-inductor-current transfer functions of peak-current-mode controlled DC-DC PWM buck converter in CCM,' in *Proc. IEEE ISCAS*, 2010, pp. 2734-2737.

[18] G. C. Verghese, C. A. Bruzos, and K. N. Mahabir, 'Averaged and sampled-data models for current mode control: Reexamination,' in *Proc. IEEE PESC*, 1989.

[19] D. J. Perreault and G. C. Verghese, 'Time-varying effects and averaging issues in models for current-mode control,' *IEEE Trans. Power Electron.*, vol. 12, no. 3, pp. 453-461, May 1997.
[20] C. P. Schultz, 'A unified model of constant frequency switching regulators using multiloop feedback control,' in *Proc. Power Conversion Conf.*, 1993, pp. 319-329.
[21] J. Sun and R. M. Bass, 'A new approach to averaged modeling of PWM converters with current-mode control,' in *Proc. IEEE IECON*, 1997, pp. 599-604.
[22] J. Sun and B. Choi, 'Averaged modeling and switching instability prediction for peak-current control,' in *Proc. IEEE PESC*, 2005, pp. 2764-2770.
[23] T. Suntio, M. Hankaniemi, and T. Roinila, 'Dynamical modeling of peak-current-mode-controlled converter in continuous conduction mode,' *J. Simul. Modeling Pract. Theory*, vol.15, no. 10, pp. 1320-1337, Nov. 2007.
[24] M. Karppanen, J. Arminen, T. Suntio, et al., 'Dynamical modeling and characterization of peak-current-mode-controlled superbuck converter,' *IEEE Trans. Power Electron.,* vol. 23, no. 3, pp. 1370-1380, May 2008.
[25] J. Huusari, J. Leppäaho, and T. Suntio, 'Dynamic properties of PCM-controlled superbuck converter – Discrete vs. coupled inductor implementation,' *Eur. Power Electron. Drives J. (EPE Journal)*, vol. 20, no. 2, pp. 8-15, Jun. 2010.
[26] J. Leppäaho and T. Suntio, 'Characterizing the dynamics of peak-current-mode controlled buck-power-stage converter in photovoltaic applications,' *IEEE Trans. Power Electron.*, vol. 28, no. 7, pp. 3840-3847, Jul. 2014.
[27] F. C. Lee and R. A. Carter, 'Investigation of stability and dynamic performances of switching regulators employing current-injected control,' in *Proc. IEEE PESC*, 1981, pp. 3-16.
[28] T. Suntio, 'Analysis and modeling of peak-current-mode controlled buck converter in DICM,' *IEEE Trans. Ind. Electron.*, vol. 48, no. 1, pp. 127-135, Feb. 2001.
[29] R. Redl, 'High-frequency extension of small-signal model of the constant-frequency current-mode-controlled converter,' in *Proc. IEEE APEC*, 1991, pp. 466-472.
[30] S. Vesti, T. Suntio, J. A. Oliver, et al., 'Effect of control method on impedance-based interactions in a buck converter,' *IEEE Trans. Power Electron*., vol. 28, no. 11, pp. 5311-5322, Nov. 2013.
[31] M. Hankaniemi and T. Suntio, 'Small-signal models for constant-current regulated converters,' in *Proc. INTELEC*, 2006, pp. 2037-2042.
[32] T. Roinila, T. Helen, M. Vilkko, T. Suntio, and H. Koivisto, 'Circular correlation based identification of switching power converter with uncertainty analysis using fuzzy density approach,' *J. Simul. Modeling Pract. Theory*, vol.17, no. 6, pp. 1043-1058, Jul. 2009.
[33] T. Roinila, M. Vilkko, and T. Suntio, 'Fast loop gain measurement of switched-mode converter using binary signal with specified Fourier amplitude spectrum,' *IEEE Trans. Power Electron.*, vol. 24, no. 12, pp. 2746-2755, Dec. 2009.
[34] R. D. Middlebrook and S. Ćuk, 'A general unified approach to modeling switching-converter power stages,' *Int. J. Electron.*, vol. 42, no. 6, pp. 521-550, Jun. 1977.
[35] T. Suntio, 'Unified average and small-signal modeling of direct-on-time control,' *IEEE Trans. Ind. Electron.*, vol. 53, no. 1, pp. 287-295, Feb. 2006.
[36] D. M. Mitchell, 'Pulsewidth modulator phase shift,' *IEEE Trans. Aerosp. Electron. Syst.*, vol. AES-16, no. 3, pp. 272-278, May 1980.
[37] T. Suntio, *Dynamic Profile of Switched-Mode Converter*, Weinheim, Germany:Wiley-VCH, 2009.
[38] T. Suntio and J. Kivimäki, 'Physical insight into the factors affecting the load-transient response of a buck converter,' in *Proc. EPE ECCE EUROPE*, 2014, pp. 1-10.
[39] V. Vorpérian, 'Simplified analysis of PWM converters using switch Part I: Continuous conduction mode,' *IEEE Trans. Aerosp. Electron. Syst.*, vol. 26, no. 3, pp. 490-496, May 1990.
[40] V. Vorpérian, 'Simplified analysis of PWM converters using switch Part II: Discontinuous conduction mode,' *IEEE Trans. Aerosp. Electron. Syst.*, vol. 26, no. 3, pp. 497-505, May 1990.
[41] R. M. Bass, Large-Signal Tools for Power Electronics: State-Space Analysis and Averaging Theory, PhD Dissertation, University of Illinois at Urbana-Campaign, 1990.
[42] C. K. Tse, *Complex Behavior of Switching Power Converters*, Boca Raton, FL, USA; CRC Press, 2004.
[43] Y. Chen, C. K. Tse, S.-S. Qiu, L. Lindemüller, and W. Schwarz, 'Coexisting fast-scale and slow-scale instability in current-mode controlled DC/DC converters: Analysis, Simulation and Experimental results,' *IEEE Trans. Circuits Syst. I, Reg. Papers*, vol. 55, no. 10, pp. 3335-3348, Nov. 2008.
[44] C.-C. Fang and R. Redl, 'Subharmonic instability limits for the peak-current-controlled buck converter with closed voltage feedback loop,' *IEEE Trans. Power Electron*., vol. 30, no. 2, pp. 1085-1092, Feb. 2015.
[45] C.-C. Fang and R. Redl, 'Subharmonic instability limits for the peak-current-controlled buck converter with closed voltage feedback loop,' *IEEE Trans. Power Electron*., vol. 32, no. 5, pp. 4048-4055, May 2017.
[46] C.-C. Fang, 'Closed-form critical conditions of subharmonic oscillations for buck converters,' *IEEE Trans.* Circuits *Syst. I, Reg. Papers*, vol. 60, no. 7, pp. 1967-1974, Jul. 2013.

Teuvo Suntio (M'98–SM'08) received the M.Sc. and Ph.D. degrees in electrical engineering from the Helsinki University of Technology, Espoo, Finland, in 1981 and 1992, respectively.

From 1977 to 1991, he worked at Fiskars Power Systems as a Design Engineer, and R&D Manager. From 1991 to 1992, he worked at Ascom Energy Systems as an R&D Manager. From 1992 to 1994 he was an entrepreneur in power electronics design consultancy, and from 1994 -1998 he worked at Efore as a Consultant, and Project Manager. Since 1998 he has been a Professor specializing in switched-mode power converter technologies first at the University of Oulu, Electronics Laboratory, and from August 2004 at the Tampere University of Technology, Department of Electrical Engineering. His current research interests include dynamic modeling, and control design of switched-mode power converters in DC-DC systems as well as in grid-connected renewable energy applications. He holds several international patents and has authored or co-authored more than 240 international scientific journal and conference papers, two books 'Dynamic Profile of Switched-Mode Converter – Modeling, Analysis and Control,' Wiley-VCH, Weinheim, Germany, 2009, and 'Power Electronic Converters – Dynamics and Control in Conventional and Renewable Energy Applications' Wiley-VCH, Weinheim, Germany, 2017 as well as two book chapters.

Prof. Suntio is a member of IEEE Power Electronics, IEEE Industrial Electronics, and IEEE Power and Energy Societies. From the beginning of 2010 he has served as an Associate Editor in IEEE Transaction on Power Electronics. He served also as the quest editor-in-chief of the special issue on power electronics in photovoltaic applications of IEEE Trans. on Power Electronics in 2011-2012. Since September 2013, he has been also a member of the editorial board of IET Circuits, Devices & Systems Journal.